














Extremely luminous optical afterglow of a distant and energetic gamma-ray burst GRB 230204B

RAHUL GUPTA ^{1,2} JUDITH RACUSIN ¹ VLADIMIR LIPUNOV ³ Y.-D. HU ^{4,5} ASHNA GULATI ^{6,7,8}
ALBERTO J. CASTRO-TIRADO ^{5,9} TARA MURPHY ^{6,7} MOTOKO SERINO,¹⁰ KIRILL ZHIRKOV,³ S. SHILLING ^{11,1,12}
SAMANTHA R. OATES ¹¹ JAMES K. LEUNG ^{13,14,15} T. PARSOTAN ¹ AMIT K. ROR ¹⁶ SHASHI B. PANDEY,¹⁶
S. IYYANI ^{17,18} V. SHARMA ¹ A. ARYAN ¹⁹ JIN-MING BAI,²⁰ PAVEL BALANUTSA,³ DAVID BUCKLEY ^{21,22}
MARÍA D. CABALLERO-GARCÍA ⁵ I. M. CARRASCO-GARCÍA,²³ A. CASTELLÓN,²⁴ SEBASTIÁN CASTILLO,²⁵
CHEN-ZHOU CUI,²⁶ YU-FENG FAN,²⁰ EMILIO FERNÁNDEZ-GARCÍA ⁵ GUILLERMO GARCÍA-SEGURA,^{27,5}
MARIA GRITSEVICH ^{28,29,30} SERGIY GUZİY ^{5,31,32} DAVID HIRIART ²⁷ WILLIAM H. LEE ³³ SOOMIN JEONG ³⁴
CARLOS JESUS PÉREZ DEL PULGAR,³⁵ IGNACIO OLIVARES,⁵ IL H. PARK ³⁶ IGNACIO PÉREZ-GARCÍA ⁵
S. RAZZAQUE ^{37,38,39} RUBÉN SÁNCHEZ-RAMÍREZ ⁵ NATALY TIURINA,³ VLADISLAV TOPOLEV,³ CHUAN-JUN WANG,²⁰
SI-YU WU ⁵ YU-XIN XIN,²⁰ DING-RONG XIONG ²⁰ XIAO-HONG ZHAO,²⁰ JIRONG MAO,²⁰ BAO-LI LUN,²⁰ AND YE KAI²⁰

¹*Astrophysics Science Division, NASA Goddard Space Flight Center, Mail Code 661, Greenbelt, MD 20771, USA*

²*NASA Postdoctoral Program Fellow*

³*Lomonosov Moscow State University, 119234, Moscow, Universitetskiiy prospect, 13, 37, Russia*

⁴*INAF-Osservatorio Astronomico di Brera, Via E. Bianchi 46, 23807 Merate, LC, Italy*

⁵*Instituto de Astrofísica de Andalucía (IAA-CSIC), Glorieta de la Astronomía s/n, E-18008, Granada, Spain*

⁶*Sydney Institute for Astronomy, School of Physics, The University of Sydney, NSW 2006, Australia*

⁷*ARC Centre of Excellence for Gravitational Wave Discovery (OzGrav), Hawthorn, VIC 3122, Australia*

⁸*CSIRO Space and Astronomy, PO Box 76, Epping, NSW 1710, Australia*

⁹*Ingeniería de Sistemas y Automática, Universidad de Málaga, Unidad Asociada al CSIC por el IAA, Escuela de Ingenierías Industriales, Arquitecto Francisco Peñalosa, 6, Campanillas, 29071 Málaga, Spain*

¹⁰*Department of Physical Sciences, Aoyama Gakuin University, 5-10-1 Fuchinobe, Chuo-ku, Sagami-hara, Kanagawa 252-5258, Japan*

¹¹*Department of Physics, Lancaster University, Lancaster, LA1 4YB, UK*

¹²*Center for Research and Exploration in Space Science and Technology, NASA Goddard Space Flight Center, Greenbelt, MD, 20771, USA*

¹³*David A. Dunlap Department of Astronomy and Astrophysics, University of Toronto, 50 St. George Street, Toronto, ON M5S 3H4, Canada*

¹⁴*Dunlap Institute for Astronomy and Astrophysics, University of Toronto, 50 St. George Street, Toronto, ON M5S 3H4, Canada*

¹⁵*Racah Institute of Physics, The Hebrew University of Jerusalem, Jerusalem 91904, Israel*

¹⁶*Aryabhata Research Institute of Observational Sciences (ARIES), Manora Peak, Nainital-263002, India*

¹⁷*Indian Institute of Science Education and Research, Thiruvananthapuram, Kerala, India, 695551*

¹⁸*High Performance Computing Centre, IISER Thiruvananthapuram, Kerala, India, 695551*

¹⁹*Graduate Institute of Astronomy, National Central University, 300 Jhongda Road, 32001 Jhongli, Taiwan*

²⁰*Yunnan Observatories, Chinese Academy of Sciences, Kunming 650216, China*

²¹*AAA Department of Astronomy, University of Cape Town, Private Bag X3, Rondebosch 7701, South Africa*

²²*AAB South African Astronomical Observatory, PO Box 9, 7935 Observatory, Cape Town, South Africa*

²³*Sociedad Malagueña de Astronomía, República Argentina 2, 29071 Málaga, Spain*

²⁴*Department of Algebra, Geometry and Topology, Facultad de Ciencias, Universidad de Málaga, Boulevard Luis Pasteur, sn, E-29071, Málaga, Spain*

²⁵*Servicios Centrales de Investigación, Universidad de Málaga, Boulevard Luis Pasteur, s/n, E-29071, Málaga, Spain*

²⁶*Beijing National Astronomical Observatory, Beijing, China*

²⁷*Instituto de Astronomía, Universidad Nacional Autónoma de México, Carr. Tijuana-Ensenada km.107, 22860 Ensenada, B.C., Mexico*

²⁸*Swedish Institute of Space Physics (IRF), Bengt Hultqvists väg 1, 981 92 Kiruna, Sweden*

²⁹*University of Helsinki, Faculty of Science, Gustav Hällströmin katu 2, FI-00014, Finland*

³⁰*Institute of Physics and Technology, Ural Federal University, Mira str. 19, 620002 Ekaterinburg*

³¹*Petro Mohyla Black Sea National University, Mykolaiv 54000, Ukraine*

³²*Mykolaiv Astronomical Observatory, Mykolaiv 54030, Ukraine*

Corresponding author: Rahul Gupta

rahulbhu.c157@gmail.com, rahul.gupta@nasa.gov

³³*Instituto de Astronomía, Universidad Nacional Autónoma de México, Apdo Postal 70-264, Cd. Universitaria, 04510 México DF, México*

³⁴*Agency for Defense Development, Daejeon 34060, Republic of Korea*

³⁵*Unidad Asociada al CSIC Departamento de Ingeniería de Sistemas y Automática, Escuela de Ingenierías, Universidad de Málaga, C. Dr. Ortiz Ramos s/n, 29071 Málaga, Spain*

³⁶*Department of Physics, Sungkyunkwan University, Seobu-ro 2066, Suwon, 16419 Korea*

³⁷*Centre for Astro-Particle Physics (CAPP) and Department of Physics, University of Johannesburg, PO Box 524, Auckland Park 2006, South Africa*

³⁸*Department of Physics, The George Washington University, Washington, DC 20052, USA*

³⁹*National Institute for Theoretical and Computational Sciences (NITheCS), Private Bag X1, Matieland, South Africa*

(Received December, 2024)

ABSTRACT

Robotic telescope networks play an important role in capturing early and bright optical afterglows, providing critical insights into the energetics and emission mechanisms of GRBs. In this study, we analyze GRB 230204B, an exceptionally energetic and multi-pulsed long GRB, detected by the *Fermi* GBM and MAXI detectors, with an isotropic equivalent gamma-ray energy exceeding 10^{54} erg. Time-resolved spectral analysis reveals a transition in the prompt emission from hard (sub-photospheric dominated) spectra during early pulses to softer (synchrotron radiation dominated) spectra in later pulses, indicative of a hybrid jet composition. We report the discovery and characterization of the optical afterglow using the MASTER and BOOTES robotic telescope networks, alongside long-term radio observations extending to 335 days post-burst with the ATCA. At ~ 1.3 ks post-burst, the optical luminosity was exceptionally high, surpassing even other bright GRBs, such as GRB 221009A (the “BOAT”). Multi-wavelength modeling, incorporating data from MASTER, BOOTES, DOT, *Swift*/XRT, and radio observations, was conducted using an external ISM forward-shock top-hat jet model with `afterglowpy`. The results reveal a narrow and highly collimated jet with a circumburst density of $n_0 \sim 28.12 \text{ cm}^{-3}$, kinetic energy $E_K \sim 4.18 \times 10^{55}$ erg, and a relatively low value of $\epsilon_B = 2.14 \times 10^{-6}$, indicating shock-compression of magnetic field in the surrounding interstellar medium. We constrained a low radiative efficiency of ~ 4.3 %. This study highlights the indispensable contribution of robotic networks to early afterglow observations and advances our understanding of GRB 230204B unique characteristics and underlying jet physics.

Keywords: Gamma-ray bursts

1. INTRODUCTION

Gamma-ray bursts (GRBs) are among the most energetic events in the Universe, emitting vast amounts of energy within a few seconds to minutes, often followed by an afterglow that can be observed across the electromagnetic spectrum (Piran 1999; Kumar & Zhang 2015). The discovery of afterglows in the late 1990s marked a significant milestone in GRB research, enabling precise localization and redshift determination, which, in turn, provided insights into the distances and energies involved (Costa et al. 1997; van Paradijs et al. 1997; Frail et al. 1997). The study of GRB afterglows, particularly in the optical regime, has been pivotal in understanding the progenitor systems, the environment surrounding the burst, and the mechanisms driving the emission (Kann et al. 2010; Li et al. 2012; Gupta 2023). The temporal evolution of these afterglows, often characterized

by a power-law decay, can reveal crucial details about the jet dynamics, energy injection, and interaction with the surrounding medium (Meszaros & Rees 1997a; Sari et al. 1998).

In recent times, robotic telescope networks, such as Mobile Astronomical System of Telescope-Robots (MASTER), Burst Observer and Optical Transient Exploring System (BOOTES), and others, have become indispensable in the rapid follow-up of GRBs, often identifying optical afterglows within minutes to hours (especially for *Fermi* Gamma-ray Burst Monitor (GBM) detected GRBs with large error circles) of the initial burst (Lipunov et al. 2010a; Castro-Tirado et al. 2012). *Fermi* GBM’s localization accuracy, while adequate for high-energy studies, often leaves large localization uncertainties spanning a few to tens of degrees radius, making rapid and wide-field follow-up observations essential.

These robotic telescope networks, equipped with wide-field cameras and fully automated systems, are specifically designed to address this challenge. Their ability to quickly respond to GRB alerts and scan large areas of the sky allows them to pinpoint transient optical emissions within the *Fermi* error regions. Additionally, their prompt response times enable them to observe early afterglow phases, providing data at these early times critical for informing the onset and evolution of the emission (Gupta et al. 2021b; Ror et al. 2023b; Sánchez-Ramírez et al. 2024). While these observations are useful for constraining GRB redshifts indirectly by identifying afterglow candidates for follow-up spectroscopic studies, they typically rely on single-band detections and are limited in sensitivity, restricting their ability to detect only the bright afterglows. Despite these limitations, the robotic nature of these observatories ensures continuous and autonomous temporal coverage, improving the chances of detecting GRBs in real-time and providing crucial data to guide further multi-wavelength follow-up efforts (Castro-Tirado 2023).

GRB 230204B, detected by the *Fermi* GBM and MAXI, stands out as one of the most energetic GRBs observed, with an isotropic equivalent energy ($E_{\gamma,iso}$) exceeding 10^{54} erg. The optical afterglow of this burst was discovered by the MASTER and BOOTES robotic telescope networks approximately 1.3 ks post-burst, marking the beginning of the broadband follow-up campaign. Additionally, at the time of MASTER/BOOTES detection (~ 1.3 ks post-burst), the optical luminosity was found to be exceptionally high when compared to other bright bursts, suggesting that GRB 230204B harbored an extremely luminous afterglow phase. In this paper, we present a detailed analysis of the optical and multi-wavelength follow-up observations (see Section 2) of GRB 230204B, including data from MASTER, BOOTES, Devasthal Optical Telescope (DOT), *Swift* Ultraviolet and Optical telescope (UVOT) and radio telescope. We explore the temporal and spectral characteristics of the prompt emission and afterglow and compare its optical luminosity with other known GRBs, the results are presented in Section 3. Discussion on potential physical mechanisms driving this energetic burst and the afterglow brightness comparison are given in Section 4. The key findings are summarized in Section 5.

2. OBSERVATIONS AND DATA ANALYSIS

This section details the observation campaign for GRB 230204B, observed by multiple space-based and ground-based telescopes across a broad wavelength range, from gamma rays to radio frequencies. Compre-

hensive details of the observing campaign are provided below and the sequence of prompt and afterglow observations for GRB 230204B is shown in Figure 1.

2.1. Prompt Emission

GRB 230204B was first detected on 4th February 2023 by the *Fermi* satellite at 21:44:27.20 UT (hereafter T_0), with T_{90} duration of 216 seconds in 50-300 keV (Poolakkil et al. 2023). MAXI also detected it at 21:47:51 UT and the burst position was constrained to approximately RA = 13h 10m 19s, Dec = $-21^\circ 45' 07''$ (J2000) with a statistical uncertainty region of 0.1° (Serino et al. 2023). The burst did not trigger the Neil Gehrels *Swift* Observatory; henceforth *Swift* (Gehrels et al. 2004). However, following the MAXI trigger notification, the Gamma-ray Urgent Archiver for Novel Opportunities (GUANO, Tohuvavohu et al. 2020) pipeline requested data from the onboard buffer of the *Swift* Burst Alert Telescope (BAT) and initiated a search within the 200-second event mode data centered around T_0 . The GRB was detected in this *Swift*/BAT GUANO data, determining its T_{90} to be approximately 65 seconds (Kennea et al. 2023). The burst was also detected by the Indian multiwavelength satellite *AstroSat*, which measured a T_{90} of $216_{-22.56}^{+5.13}$ seconds (Waratkar et al. 2023). The prompt emission of the burst was also seen by *AGILE* (Casentini et al. 2023) and *GRBAlpha* (Dafnikova et al. 2023) missions, with every mission providing a slightly different value of T_{90} duration as expected due to the different sensitive and spectral coverage.

2.2. Prompt X-ray Emission: MAXI

MAXI (mounted on the *ISS*) scans a position of the sky every 92 minutes (Matsuoka et al. 2009). The position of the GRB moved into the MAXI field of view at $T_0 + 192.8$ sec, and the scan transit ended at $T_0 + 248.8$ sec. During the scan transit, the MAXI/GSC nova alert system (Negoro et al. 2016) triggered the burst at 21:47:51 UT ($T_0 + 203.8$ sec), with MAXI's detection revealing the soft nature of the burst. Assuming the source flux was constant over the transit, the X-ray flux in the 4.0–10.0 keV band was calculated to be 628 ± 49 mCrab (1 sigma error, Serino et al. 2023).

After the detection of prompt emission, MAXI/GSC could not observe the position of the burst for about 6 hours due to the observation constraint of the radiation zone (Sugizaki et al. 2011) in the International Space Station (ISS) orbit. The observation resumed at $\sim T_0 + 22.5$ ks, and there were 11 consecutive scan transits before the start of the observations by *Swift*/XRT. The afterglow was not detected in any transit. We calculated 3 sigma upper limits in the 2–20 keV band (see Table

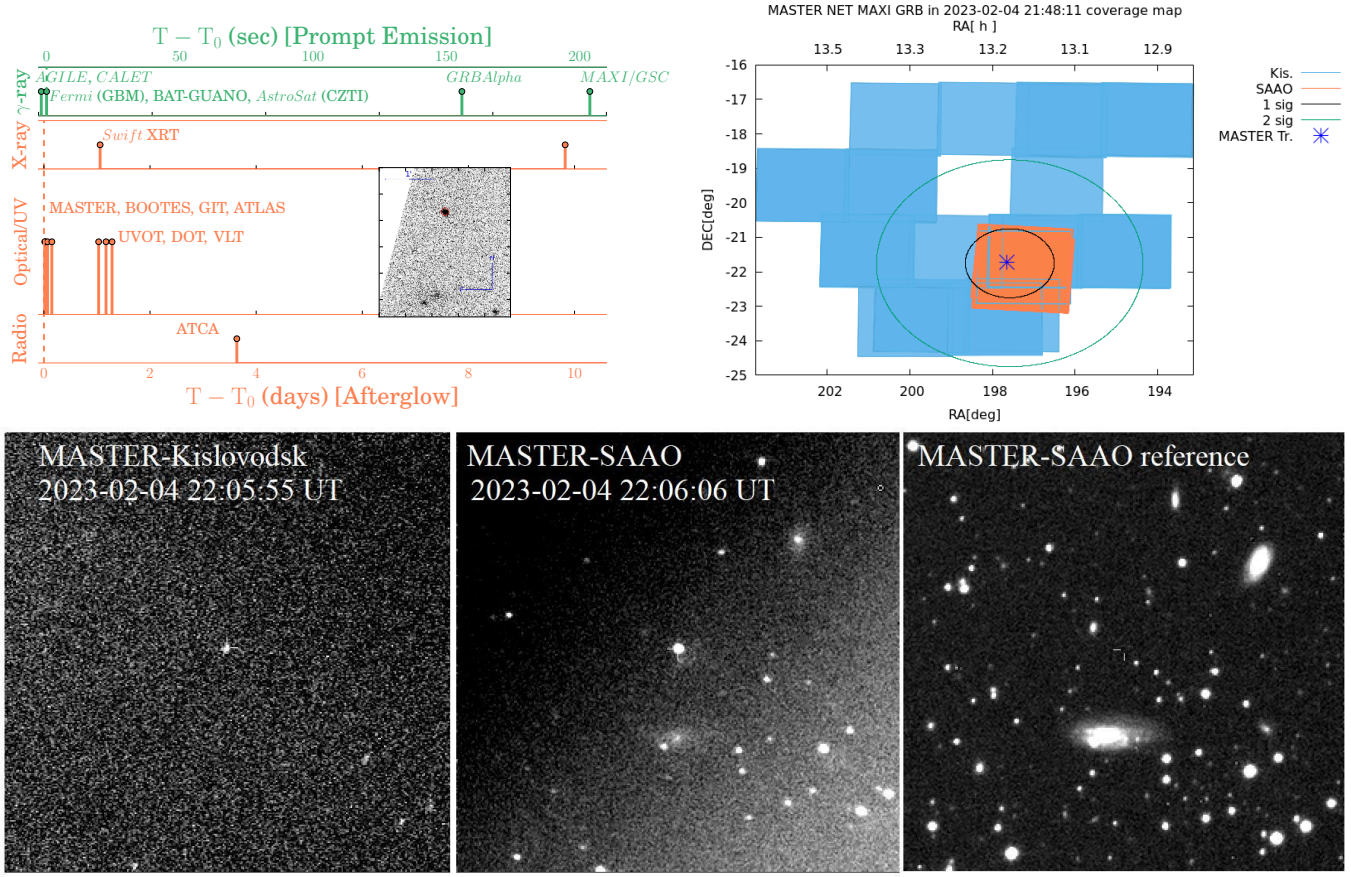


Figure 1. Top left: Sequence of prompt and afterglow observations for GRB 230204B, the dashed vertical line indicating the *Fermi*-GBM trigger time. Vertical green and orange lines with dots correspond to the start times of observations by respective instruments. The inset shows the BOOTES finding chart, based on the optical discovery image of the burst. Top right: Coverage map of the MASTER network observations for the MAXI-detected GRB 230204B. The regions observed by the MASTER-Kislovodsk (blue squares) and MASTER-SAAO (orange squares) are shown, overlaid with 1-sigma (black ellipse) and 2-sigma (green ellipse) positional uncertainties of the GRB location. The blue star indicates the MASTER transient (MASTER Tr.) detection, situated near the center of the 1-sigma error region. Bottom left: Optical finding chart for GRB 230204B from observations taken by MASTER-Kislovodsk, MASTER-SAAO (Bottom middle), and a reference MASTER-SAAO image (Bottom right). The afterglow position is marked with crosshairs in each image.

A5 in appendix) for these transients following the method by Sugita et al. (2018).

2.3. Afterglow: Soft X-ray Emission

The fading X-ray counterpart of GRB 230204B was detected by *Swift*/XRT approximately 80 ks after the burst trigger (D’Elia et al. 2023). Given the faint nature of the X-ray afterglow at such a late epoch, all observations were performed in photon counting (PC) mode to optimize sensitivity for faint sources. Follow-up observations were conducted during two epochs (XRT exposure times of 5.1 ks, and 4.5 ks, respectively), on 5 February 2023 and 14 February 2023, resulting in only two usable data points (see Table A2 of the appendix). The final observation on February 14 approached the detection limit of the instrument, emphasizing the faintness

of the X-ray emission and the challenges of constraining the X-ray afterglow’s properties at these late times.

2.4. Afterglow: Optical Emission

We discovered the optical afterglow of GRB 230204B using two robotic telescope networks (using MASTER in the unfiltered band and using BOOTES in the clear band, respectively) independently (see Figure 1). The optical counterpart of the burst was also identified by the 0.7m GROWTH-India Telescope (GIT) approximately 1.57 hours (later than MASTER and BOOTES) after the burst trigger (Swain et al. 2023). This optical afterglow was subsequently observed by several other ground-based telescopes (Smartt et al. 2023; Ror et al. 2023a). The redshift of the burst, $z = 2.142$, was determined through spectroscopic observations using the X-shooter spectrograph on the Very Large Telescope (VLT,

Saccardi et al. 2023). The given magnitude (for the positive detection) and upper limits within 3σ are listed in Table A3.

2.4.1. MASTER robotic telescope

MASTER global network consists of 9 identical fully robotic wide-field twin telescopes with 4-8 square degrees field of view, distributed around the Earth for all-sky monitoring up to 19-20 mag with the goal of detecting optical transients, including high energy astrophysics events such as GRBs, Gravitational waves, ultra-high energy neutrino and Fast Radio Bursts (Lipunov et al. 2010b, 2019, 2022, 2023). We observed such events as soon as possible upon receiving the alerts (Ershova et al. 2020) using the GCN system (Barthelmy et al. 1998; Barthelmy 2003, 2016) every night in both, the fully robotic open (8 square degrees FOV) and closed (4 square degrees FOV) modes, being ready for observations with fully clear hemisphere (clamshell dome constructions). Open mode is used in the case of alerts provided by *Fermi*, LIGO/Virgo, IceCube, ANTARES/KM3Net (with large error boxes) when at least 2 images per night are required if large error boxes are at least 5 degrees above the horizon, in order to cover as much as possible with our given field of view. Closed mode (using both tubes in parallel Kornilov et al. (2012)) is preferred for events with error boxes smaller than 1 degree such as the ones provided by *Swift*, MAXI, *Fermi*-LAT, GECAM, *Einstein Probe*, INTEGRAL, when polarization observations can be undertaken (Troja et al. 2017; Jordana-Mitjans et al. 2020; Gupta et al. 2022a). The first exposure duration also depends on the time between the trigger and the start of observation and can be increased from 10 sec at the first minute to 180 sec at later stages in order to detect the fainter objects.

GRB 230204B was observed by MASTER-Kislovodsk and MASTER-SAAO. First images were received for the MAXI error box, then telescopes automatically pointed to *Fermi* field. The MASTER-Kislovodsk robotic telescope started observing the MAXI trigger 979708795 observation at 2023-02-04 22:05:55 UT (1064 sec after trigger time which was 74 sec after the notification time, see Figure 1) at 11° altitude, in 44° distance to the Moon (0.3 phase, that creates significant interference for wide-field instruments observations) through clouds at horizon with $m_{lim}=14.8$ mag at first image in polarization filter.

The MASTER-SAAO robotic telescope located in the South African Astronomical Observatory, started observing error box automatically 85 seconds after notice time (i.e. 1075 sec after trigger time) at 2023-

02-04 22:06:06 UT with optical counterpart MASTER OT J131034.94-214304.8 detection, coincident with the counterpart reported by GIT, ATLAS, VLT, DOT, and BOOTES¹. The observations began at 27° altitude with an exposure time of 180 sec in the polarization filter. The OT unfiltered magnitude in the first image was 12.9 mag ($m_{lim}=17.6$ mag). We used a reference image on 2020-04-24.82 UT with unfiltered $m_{lim}=20.6$ mag.

For the photometric analysis of this object, catalog data for comparison stars were sourced from Gaia EDR3 to evaluate the variance in magnitude errors. The photometry dataset excludes frames where the comparison star data were deemed unreliable. The magnitude error for comparison stars was computed as the deviation between the weighted average magnitude (where weights are the inverse square of the signal-to-noise ratio) and the magnitude measured on individual frames. Two approaches were employed to determine the stellar magnitude. In the first approach, a reference star from Gaia EDR3 was identified, its flux on the observational frame measured, and the magnitude calculated using Pogson's scale. In the second approach, a zero-point correction was applied to the reference star's magnitude, utilizing the comparison stars as secondary references. The second method generally produced a smaller magnitude variance compared to the first, owing to the improved calibration achieved through the zero-point correction. This dual-approach methodology ensures robust photometric accuracy while mitigating systematic errors.

2.4.2. BOOTES robotic telescope

BOOTES followed up GRB 230204B with three of the six 60 cm robotic telescopes, namely the ones at the BOOTES-4/MET station in Lijiang Astronomical Observatory (Yunnan, China), at BOOTES-5/JGT station in Observatorio Astronómico Nacional of San Pedro Mártir (Baja California, México) and at the BOOTES-2/TELMA station in La Mayora (Málaga, Spain). Following the MAXI trigger, the BOOTES-4/MET telescope performed two epoch observations at 2023-02-04 22:19:12 UT and 2023-02-05 17:42:04 UT. The BOOTES-2/TELMA telescope and the BOOTES-5/JGT telescope also executed follow-up observations at 2023-02-05 04:16:55 UT and 2023-02-05 07:43:45 UT, respectively. A series of images were obtained using the clear filter with exposures of 1 sec, 5 sec, and 10 sec at BOOTES-4/MET telescope during the first epoch and the optical afterglow was clearly detected during the decaying phase. However, during the following multi-filters (Sloan-*riz* and clear filters, 60 sec exposure) mon-

¹ <https://gcn.gsfc.nasa.gov/other/230204B.gcn3>

itoring, the optical afterglow was not detected on the stacked images for each epoch (as they were not as deep as the clear filter exposures). All the images were processed with bias, dark subtraction, and flat-field correction using custom IRAF routines (Gupta et al. 2021b). Photometry was carried out using the standard IRAF package and the images were calibrated with nearby comparison stars from the USNO-B1.0 and SDSS catalogs.

2.4.3. DOT

We initiated observations using the DOT (Pandey 2016; Gupta et al. 2024a) on 2023-02-06 at 01:49:47.939 UT, approximately 1.16 days after the trigger. Multiple frames with an exposure time of 180sec each were observed in the g , r , and i bands, and continuous observations were conducted over four consecutive nights using the same filters. For image preprocessing, we employed the standard IRAF framework, and DAOPHOT II was used to determine magnitudes from the cleaned files. We stacked the images for each night in the same filter to increase the signal-to-noise ratio. PSF photometry was performed on the final stacked images (Gupta et al. 2022b,c). Due to the high moon phase during the burst observation, we only detected GRB 230204B in the r and i -band images from the first night. For the remaining filters, we could only establish upper limits. Photometric calibration is performed using the standard stars from the Pan-STARRS catalog.

2.4.4. *Swift*/UVOT

The *Swift*/UVOT began settled observations of the field of GRB 230204B 80.6ks after the MAXI trigger (Serino et al. 2023). No optical afterglow was detected by UVOT. Photometry was obtained from co-added UVOT image mode data. The source counts were extracted from the UVOT stacked images using a source region of 5 arcsec radius. Background counts were extracted using an aperture of 20 arcsec in radius located in a source-free region near the GRB. We use the *Swift* tool `uvotsource` to obtain the background subtracted count rates using source and background apertures of 5 and 20 arcseconds in radius, respectively. They were converted to magnitude using the UVOT photometric zero points (Breeveld et al. 2011; Poole et al. 2008).

2.4.5. Radio Emission

We observed GRB 230204B on 8 February 2023 (3.6 days post-burst), with the Australia Telescope Compact Array (ATCA, Project code CX527) at a wide range of frequencies centered on 5.5, 9.0, 16.7, 21.2, 33 and 35 GHz, each with a 2048 MHz-wide band. We reduced the visibility data using standard routines in MIRIAD

(Sault et al. 1995). We used a combination of manual and automatic RFI flagging before calibration, conducted with MIRIAD tasks `uvflag` and `pgflag`, respectively. We used PKS 1934–63 to determine the bandpass response for frequency bands 5.5 and 9 GHz, and PKS 0727–115 as the bandpass calibrator for 16.7, 21.2, 33 and 35 GHz bands. We used PKS 1934–63 to calibrate the flux density scale for all frequency bands. We used PKS 1256–220 to calibrate the time-variable complex gains for all epochs and frequency bands. After calibration, we inverted the visibilities using a robust weighting of 0.5 and then used the CLEAN algorithm (Clark 1980) on the target source field using standard MIRIAD tasks `INVERT`, `CLEAN` and `RESTOR` to obtain the final images.

We detect the radio counterpart at 16.7 and 21.2 GHz at a position consistent with the BOOTES/MASTER/GIT optical counterpart position (Swain et al. 2023). For all other frequencies, we report 5-sigma upper limits (see Table A4 of appendix). The GRB position was also observed with the Australian SKA Pathfinder by the Rapid ASKAP Continuum Survey (RACS; McConnell et al. 2020) on 2023 July 1 and 2024 Jan 5. We find no radio detections in preliminary data and report 5-sigma upper limits of 1.5 mJy. There were also no archival radio detection pre-burst within 1 arcminute in surveys: the National Radio Astronomy Observatory VLA Sky Survey (Condon et al. 1998), the Sydney University Molonglo Sky Survey (Mauch et al. 2003), the Very Large Array Sky Survey (Lacy et al. 2020) or the RACS survey. We measured a VLASS 5-sigma upper limit of 0.69 mJy at 3 GHz.

2.4.6. *Swift* BAT Survey Data

Swift/XRT did not observe the location of X-ray afterglow of GRB 230204B until 91.5 ks post-burst. Therefore to search for the hard X-ray early afterglow, we used the `BatAnalysis` python package (Parsotan et al. 2023) to analyze *Swift* BAT survey data from 2023-02-03 to 2023-02-11. We analyzed survey data, where the location of the GRB had at least a partial coding fraction of $\sim 19\%$ on the BAT detector plane. As expected, the GRB afterglow was not detected in the BAT survey data, which is typical since hard X-ray afterglows have never been detected at such late times. However, we were able to place 5σ upper limits on the emission in the 14-195 keV energy band (shown in Figure 2). We additionally conducted a mosaiced analysis of the BAT survey data in 1-day time bins, for two days after the trigger time, and were able to place 5σ flux upper limits on the emission in the 14-195 keV energy band where the flux of the GRB afterglow is $\lesssim 2 \times 10^{-9}$ erg/sec/cm².

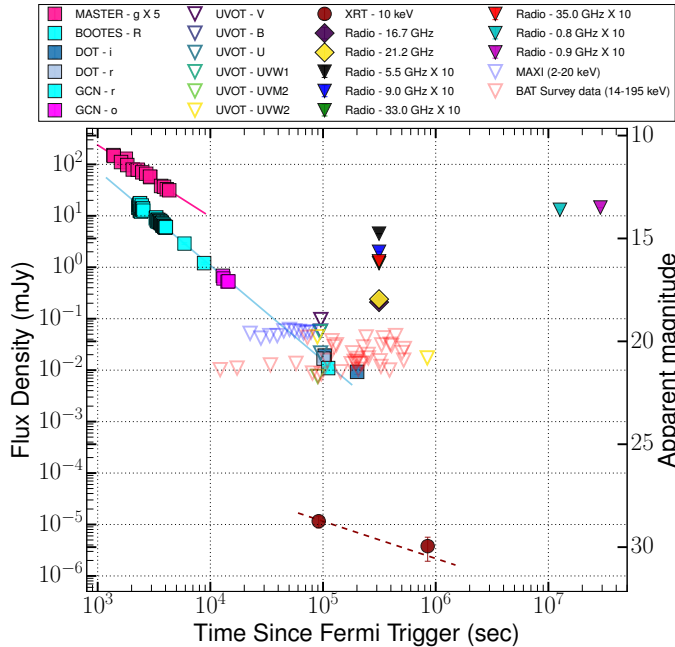


Figure 2. Broad-band composite afterglow flux density light curve of GRB 230204B. The solid lines are the best-fit power-law function to optical data (temporal decay index of -1.85 ± 0.03 in R/r band) and the dashed line shows the best-fit power-law function to X-ray data (temporal decay index of -0.72 ± 0.63). The upper limits for X-ray afterglow search using MAXI (2-20 keV) and BAT Survey data (14-195 keV) are shown using light blue and red color markers, respectively.

Based on the above observations, we have shown the broadband composite afterglow light curve of GRB 230204B in Figure 2.

3. RESULTS

3.1. Prompt emission temporal and spectral characterize

For the analysis of *Fermi* GBM data, we utilized the *Fermi* GBM Data Tools² to extract temporal information. We selected specific NaI (NaI 7 and NaI 8) and BGO (BGO 1) detectors for the analysis based on their optimal viewing angles relative to the GRB’s position to maximize the signal-to-noise ratio. For the NaI detectors, we focused on two energy bands: 8-30 keV and 50-300 keV, allowing us to explore both low and high-energy photon populations. For BGO 1, two bands were used: 0.3-1 MeV and 1-40 MeV, to investigate higher-energy photons. The prompt emission background-subtracted light curve of GRB 230204B, ob-

tained using *Fermi* GBM across different energy channels, reveals a complex multi-pulse structure, as shown in Figure 3. This GRB exhibits four distinct emission episodes, each separated by periods of quiescence, with the shaded regions highlighting the intervals selected for time-integrated spectral analysis. The energy-dependent light curves show that the temporal structure and intensity vary significantly across different energy bands, reinforcing the diverse nature of GRB light curves. Notably, the hardness ratio (HR) demonstrates evolution over time, indicating spectral changes during the burst. The inset plot shows the MAXI light curve, covering the 2-20 keV energy range, further subdivided into 2-4 keV, 4-10 keV, and 10-20 keV. Although MAXI detected only part of the GRB, its observations provide valuable insights into the lower-energy emission and suggest a very softer nature of the last pulse of GRB 230204B.

We analyzed the time-integrated ($T_0-0.80$ to $T_0+229.69$ sec) *Fermi* spectrum of GRB 230204B using the Multi-Mission Maximum Likelihood framework (3ML) to evaluate its spectral characteristics. We explore several phenomenological models, including the **Band** function, **Cutoff power-law** (CPL), and combinations with a **Blackbody** component, which is theoretically expected to originate from the photospheric emission of GRBs. For each model, we employed Bayesian spectral fitting to obtain the Deviance Information Criterion (DIC) values, allowing us to systematically compare the model fits. The results indicate that the **Band** function provides a statistically better fit to the time-integrated spectrum compared to the CPL alone, as indicated by the DIC values. Furthermore, the addition of a **Blackbody** component alongside the **Band** function yielded an even lower DIC value, suggesting that this model combination better describes the observed spectral features.

In addition to the time-integrated spectrum, we analyzed the spectral evolution across four distinct emission episodes of GRB 230204B, fitting each episode with the same set of phenomenological models. Our findings show that the first and third episodes are best described by the CPL + **Blackbody** model, while the second and fourth episodes favor the **Band** + **Blackbody** combination based on DIC values. The DIC values and the best-fit spectral parameters for both the time-integrated analysis and individual episodes are summarized in Table 1 and Table 2. These results highlight the diversity in spectral shapes across the burst duration and provide valuable insights into the complex emission mechanisms underlying GRB 230204B, supporting the presence of a thermal component in combination with non-thermal models.

² https://fermi.gsfc.nasa.gov/ssc/data/analysis/gbm/gbm_data_tools/gdt-docs/

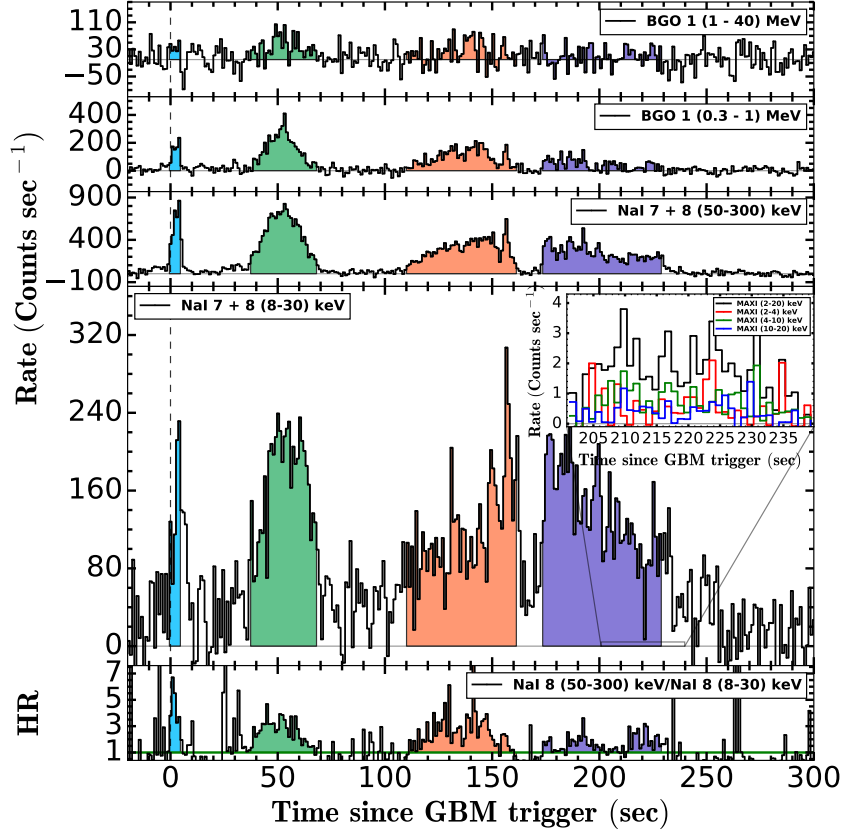


Figure 3. The prompt emission background-subtracted light curve of GRB 230204B, obtained using *Fermi* GBM across different energy channels: NaI 7+8 (8-30 keV), NaI 7+8 (50-300 keV), BGO 1 (0.3-1 MeV), and BGO 1 (1-40 MeV). The shaded regions represent the time intervals used for time-integrated spectral analysis for each of the four emission episodes. The hardness ratio (HR) evolution is shown as a function of time. The inset plot shows the MAXI light curve in 2-20 keV, 2-4 keV, 4-10 keV, and 10-20 keV energy bands, illustrating that MAXI observed only a later emission of GRB 230204B.

Table 1. The DIC values for both the time-integrated analysis and individual episodes. The boldface shows the best-fit model.

Time-intervals (from T_0 in sec)	DIC value			
	Band	CPL	BB+Band	BB+CPL
-0.80-229.69	7118.17	7123.59	7094.00	7103.16
-0.80-4.97	3245.26	3245.68	3220.72	3214.46
37.00-68.15	5083.02	5091.67	5058.11	5077.71
109.450-161.90	5655.64	5660.37	5619.57	5606.26
172.58-229.69	5601.18	5606.86	5575.45	5577.01

Table 2. The best-fit spectral parameters for both the time-integrated analysis and individual episodes.

Time-intervals (from T_0 in sec)	Best-fit parameters					
	α_{pt}	E_p (keV)	β_{pt}	Γ_{CPL}	E_c (keV)	kT (keV)
-0.80-229.69	$-0.78^{+0.03}_{-0.07}$	$519.44^{+81.71}_{-19.58}$	$-3.37^{+0.16}_{-3.58}$	—	—	$15.08^{+29.28}_{\text{unconstrained}}$
-0.80-4.97	—	—	—	$-0.38^{+0.05}_{-0.11}$	$259.10^{+56.09}_{-13.35}$	$24.98^{+24.90}_{-1.05}$
37.00-68.15	$-0.65^{+0.03}_{-0.05}$	$661.98^{+75.23}_{-21.83}$	$-2.61^{+0.18}_{-0.24}$	—	—	$15.51^{+30.46}_{\text{unconstrained}}$
109.450-161.90	—	—	—	$-0.70^{+0.01}_{-0.07}$	$514.31^{+111.17}_{-16.22}$	$14.01^{+46.29}_{-0.85}$
172.58-229.69	—	—	—	$-0.80^{+0.01}_{-0.09}$	$239.09^{+58.10}_{-2.48}$	$10.62^{+32.45}_{\text{unconstrained}}$

GRBs are known for their significant spectral evolution and high variability, with emission properties often varying notably across individual pulses within multi-pulse bursts. Li et al. (2021) conduct a comprehensive time-resolved Bayesian spectral analysis of well-defined GRB pulses observed by *Fermi*. They observe a trend toward spectral softening over time, largely reflected in the gradual decrease of the low-energy power-law index. We compared the time-resolved spectral analysis of GRB 230204B with the sample studied by Li et al. (2021). We also observe that the low-energy power-law indices of GRB 230204B become softer over time (hard to soft), with a distinct spectrum evolution from the first to later episodes (see Figure 4). Such spectral evolution feature of prompt emission could be explained as photospheric emission is most commonly observed near the trigger time, while synchrotron-like emission becomes more prevalent in later times, indicating the coexistence of multiple emission mechanisms as the burst evolves (Li et al. 2021).

3.2. Pulse-wise prompt emission correlation and analysis

The pulse-wise analysis of GRB prompt emission provides a valuable perspective on the Amati and Yonetoku correlations (key relationships used to explore the physical properties of GRBs), enhancing our understanding of GRB spectral evolution and energetics on a finer timescale (Chand et al. 2020). By examining each pulse independently, rather than averaging over the entire prompt emission phase, we gain insights into the distinct characteristics of individual emission episodes within a single burst. In the Amati correlation, which relates the isotropic energy ($E_{\gamma, \text{iso}}$) to the spectral peak energy in the rest frame (Amati 2006), each pulse may fall along or diverge from the established long and short GRB trends, providing information about the pulse-specific energy release mechanisms. Such an analysis not only clarifies the evolutionary trajectory of the GRB emission but also tests the applicability of the Amati correlation at sub-burst levels (Basak & Rao 2013).

In the top-left panel of Figure A1, we illustrate the positioning of each pulse (plotted as colored squares) of GRB 230204B within the established Amati correlation. For reference, samples of long and short bursts from Minaev & Pozanenko (2020) are represented by orange and blue circles, respectively. The linear fits corresponding to these groups are indicated by solid orange and blue lines, with 3σ uncertainties depicted by shaded bands around each fit. The time-integrated and pulse-wise analysis of GRB 230204B follows the Amati plane of long GRB populations. The top-right panel of Fig-

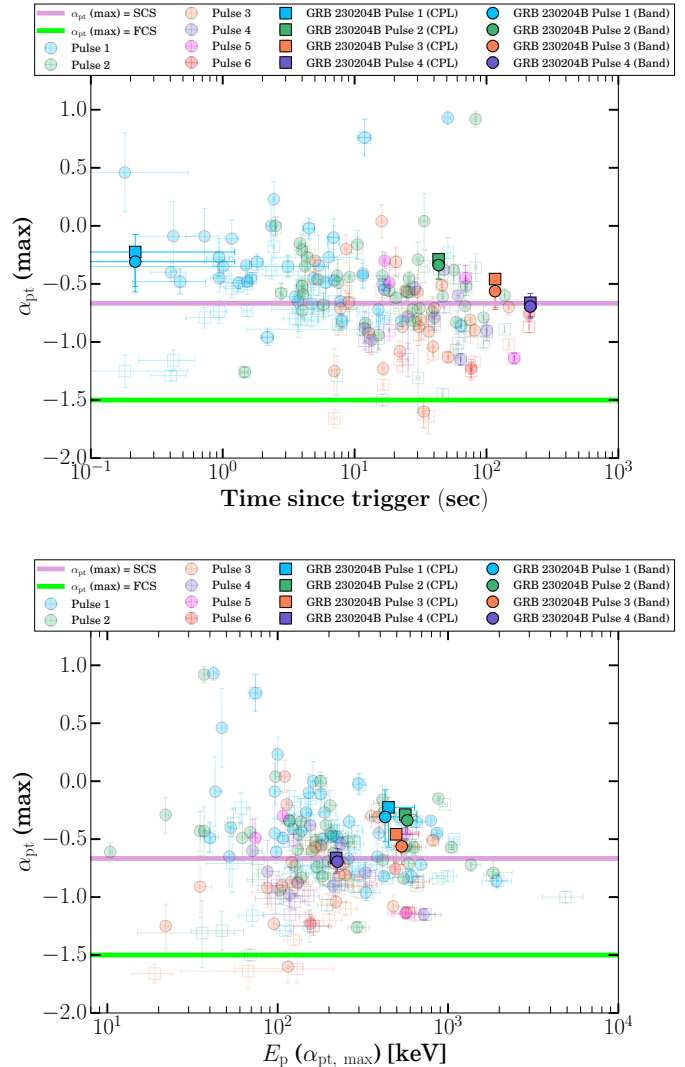


Figure 4. Spectral evolution of GRB 230204B during prompt emission detected by *Fermi* GBM. The top panel shows the evolution of the maximum value of low-energy power-law indices during each pulse of GRB 230204B as a function of trigger time. The pink and lime-colored horizontal lines show the synchrotron line of death and the fast-cooling synchrotron emission line, respectively. The bottom panel shows the evolution of the maximum value of low-energy power-law indices during each pulse of GRB 230204B as a function of peak energy corresponding to the maximum value of α . The data points for spectral parameters of individual pulses of other multi-pulsed *Fermi* GRBs obtained from Li et al. (2021), are also shown.

ure A1 presents GRB 230204B positions within the Yonetoku correlation framework, a relation between peak energy and the isotropic peak luminosity ($L_{\gamma, \text{iso}}$) in the rest frame (Yonetoku et al. 2004). Here, the short and long GRB samples from Nava et al. (2012) are shown by blue and orange circles, with the 3σ scatter around

each population’s best-fit line visualized by shaded areas. GRB 230204B follows the Yonetoku correlation and lies on the upper side of this correlation. The results in both correlations offer an insightful examination of GRB 230204B, highlighting the pulse-specific properties within established GRB behavior and indicating the energetic and luminous nature of the burst.

3.2.1. Spectral Peak-Duration Distribution Analysis

Long-duration GRBs are generally characterized by a softer spectrum relative to the typically harder spectrum observed in the majority of short-duration GRBs, as demonstrated in previous studies (e.g., Kouveliotou et al. 1993). To analyze this characteristic for GRB 230204B, we measured both the time-integrated and episode-wise spectral peak energy (an indicator of spectral hardness) alongside the T_{90} duration (the time during which 90% of the burst’s total fluence is detected, for example, T_{90} calculation for the second pulse of GRB 230204B is shown in the bottom left of Figure A1 of the appendix). We then plotted the pulse-wise values on the E_p - T_{90} plane to compare with a larger dataset of GRBs detected by the *Fermi* GBM, as illustrated in the bottom right panel of Figure A1.

Our results indicate that the time-integrated and episode-wise properties of GRB 230204B exhibit softer E_p values and durations exceeding 2 seconds, placing it on the right side of the spectral peak-energy versus duration plane. This position aligns well with the properties typically observed for long-duration GRBs, as they occupy the region in the E_p - T_{90} plane corresponding to longer durations and softer spectra. This comparison confirms that GRB 230204B follows the standard characteristics of long-duration GRBs.

3.3. Afterglow analysis and correlation

Based on the multi-wavelength follow-up observations campaign (~ 1.3 ks to 335 days post burst) of GRB 230204B, we noted that BOOTES robotic and DOT observations have a well-sampled light curve in optical R/r filters. We fitted flux density optical R/r -band light curves using a simple power-law function with a temporal decay index of -1.85 ± 0.03 ($\chi^2/\text{DOF} = 43.47/52$). Furthermore, we combined all the optical data (MASTER, BOOTES, DOT, and a few points from GCN) to get a more well-sampled light curve and it could also be fitted with a simple power-law function with a temporal decay index of -1.84 ± 0.02 ($\chi^2/\text{DOF} = 81.13/58$). We noted that the optical temporal index is steeper than the typically observed decay slope of ~ -1 (Dainotti et al. 2022). On the other hand, the X-ray afterglow light curve of GRB 230204B has very limited (close to the sensitivity of XRT) data points as

Swift followed the burst during the late phase and could be fitted with a temporal decay index of -0.72 ± 0.63 ($\chi^2/\text{DOF} = 0.58/1$).

The correlation between the average optical decay index and optical luminosity provides crucial insights into the physical mechanisms governing GRB afterglows and their surrounding environments. Oates et al. (2012, 2015) examined the possible correlation between the average optical temporal decay indices and optical luminosity (at 200-sec post burst) for GRBs with optical afterglows observed by *Swift*/UVOT. They found evidence of anti-correlation between these two parameters (200-sec post burst) as shown in Figure 5. This correlation indicates that optical luminous bursts decay more rapidly than optical faint bursts. We measured optical luminosity and temporal decay index for GRB 230204B and overlaid it onto the luminosity-decay correlation. GRB 230204B exhibits a relatively steep decay rate (~ 1.4 in MASTER g filter) and high optical luminosity (at the first epoch of afterglow detection). We noted GRB 230204B, highlighted in red in the figure, aligns well with the global correlation observed for long-duration GRBs and lies towards the edge (see Figure 5). Possible physical explanations of this correlation are discussed in section 4.2.

3.4. Broadband afterglow modeling of GRB 230204B

The broadband afterglow modeling involved fitting the observed data across multiple wavelengths, including radio, optical, and X-ray bands. Such broadband modeling helps to understand the physical parameters of the jet, such as its opening angle, energy, and the surrounding medium’s density. The afterglow emission is generally explained by the synchrotron radiation model (Sari et al. 1998; Meszaros & Rees 1997b; Sari & Piran 1999). In this model, relativistic electrons are accelerated by the GRB shockwave spiral in the magnetic field, emitting radiation across the electromagnetic spectrum. The synchrotron spectrum is characterized by several break frequencies (self-absorption, peak, and cooling frequencies), which evolve with time and affect the observed light curves at different wavelengths.

For the afterglow modeling of GRB 230204B, we utilized `afterglowpy`³ (Ryan et al. 2020)/`Redback` (Sarin et al. 2024) to explore various jet structure models, including the Tophat, Gaussian, and GaussianCore models. The Bayesian inference framework provided by `Redback` allowed us to test different priors and achieve

³ It currently does not account for certain features, including reverse shock emission, an external wind medium ($n \propto r^{-2}$), or synchrotron self-absorption.

Table 3. Physical parameters of the afterglow for GRB 230204B, derived through Bayesian fitting using the `Redback` and `afterglowpy` frameworks.

Model	Top hat	Gaussian	Gaussian Core
θ_{observer} (rad)	$0.003^{+0.002}_{-0.001}$	$0.004^{+0.002}_{-0.001}$	$0.005^{+0.001}_{-0.001}$
θ_{core} (rad)	$0.006^{+0.003}_{-0.002}$	$0.006^{+0.002}_{-0.001}$	$0.007^{+0.001}_{-0.001}$
θ_w (rad)	–	$4.020^{+2.676}_{-2.131}$	$4.714^{+1.567}_{-1.766}$
$\log_{10} E_0/\text{erg}$	$55.621^{+0.229}_{-0.262}$	$55.529^{+0.159}_{-0.187}$	$55.143^{+0.113}_{-0.150}$
p	$2.280^{+0.020}_{-0.022}$	$2.267^{+0.018}_{-0.017}$	$2.252^{+0.017}_{-0.017}$
$\log_{10} n_{\text{ism}}/\text{cm}^{-3}$	$1.449^{+1.036}_{-1.002}$	$1.987^{+0.823}_{-0.696}$	$2.685^{+0.450}_{-0.447}$
$\log_{10} \epsilon_B$	$-5.669^{+0.650}_{-0.651}$	$-5.899^{+0.500}_{-0.520}$	$-6.133^{+0.397}_{-0.318}$
$\log_{10} \epsilon_e$	$-0.525^{+0.229}_{-0.209}$	$-0.353^{+0.170}_{-0.149}$	$-0.198^{+0.102}_{-0.107}$
ξ_N	1.0	1.0	1.0
$\ln(Z)$	-101.31 ± 0.08	-107.50 ± 0.08	-110.53 ± 0.08
$\ln(\text{BF})$	7638.16	7631.97	7628.94

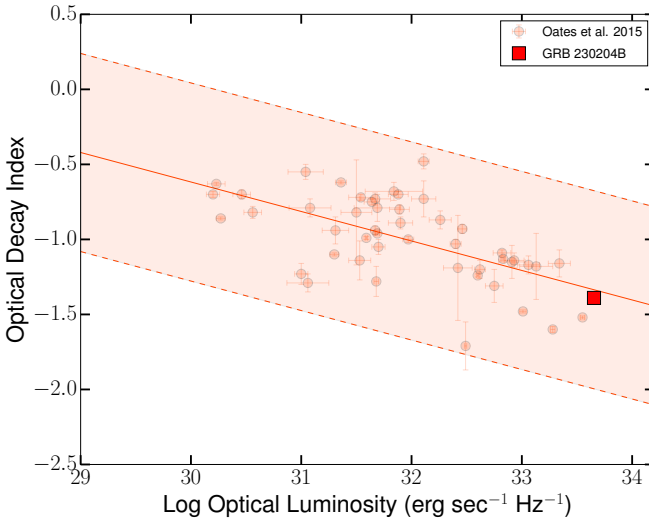


Figure 5. The correlation between the average optical decay index and optical luminosity (at 200-sec post burst) for a sample of GRBs Oates et al. (2012, 2015), with GRB 230204B highlighted in red. This plot illustrates the diverse afterglow properties of GRBs, where the decay index reflects the temporal evolution of the optical afterglow and the luminosity indicates the energy output. GRB 230204B’s position in the parameter space aligns with the general trend observed in long-duration GRBs, showcasing very high optical luminosity and a steep decay rate. The solid indicates the best-fit regression analysis for the correlation in this sample, and the shaded region represents the $3\times$ of root mean square deviation.

robust parameter estimation. Specifically, we employed the `PyMultiNest` sampler to explore the parameter space and used well-defined priors for key parameters such as the observer angle (θ_v), core angle (θ_c), initial energy (E_0), and interstellar medium density (n_{ISM}). Due to the limited number of data points, we have fixed bulk Lorentz factor ($\Gamma \sim 800$), constrained using the $E_{\gamma, \text{iso}}$ -Lorentz factor correlation (Liang et al. 2010). The

priors used in the analysis include uniform distributions for the energy, core angle, ambient medium density, and a sine prior for the observer’s viewing angle.

The Top-Hat model provided the best fit to the data (see Figure 6), with log evidence ($\ln Z$) of -101.31 ± 0.08 and a Bayes factor ($\ln \text{BF}$) of 7638.16 as indicated by the Bayesian evidence comparison. These results strongly suggest that the jet structure for GRB 230204B is best described by a simple Top-Hat profile (see Table 3). The posterior distributions (see corner plot as shown in Figure A2 of the appendix) constrained viewing angle of θ_v 0.003 rad and a core angle θ_c 0.006 rad (limit as no jet break is observed), suggesting a narrow, highly collimated jet structure. The inferred initial energy is relatively high at $\log_{10}(E_0) \sim 55.62$ erg, and the ISM density is constrained to $\log_{10}(n_{\text{ism}}) \sim 1.45 \text{ cm}^{-3}$.

The Top-Hat jet model provides a robust description of GRB 230204B’s afterglow, indicating a narrow, highly collimated jet. This is consistent with the high fluence observed in the early afterglow phase. The tightly constrained parameters for θ_v and θ_c indicate that we are likely observing the jet from a viewing angle close to the core, providing a relatively straightforward interpretation in the context of synchrotron emission from a top-hat jet model. A notable feature in the fit is the very low value of ϵ_B , the magnetic field fraction, which was constrained to $\log_{10} \epsilon_B = -5.67^{+0.65}_{-0.65}$. This low magnetic field can plausibly arise from shock compression of the ambient interstellar medium (ISM), which supports a weakly magnetized medium (Kumar & Barniol Duran 2009; Wang et al. 2015). Similar values of ϵ_B have been observed in GRBs such as GRB 190530A (Gupta et al. 2022a), GRB 171205A (Leung et al. 2021), GRB 130427A (Fraija et al. 2016), and a few others (Kumar & Barniol Duran 2009, 2010; Santana et al. 2014), highlighting the diversity in GRB environments. For GRBs, when $\epsilon_e \gg \epsilon_B$, there might be Synchrotron

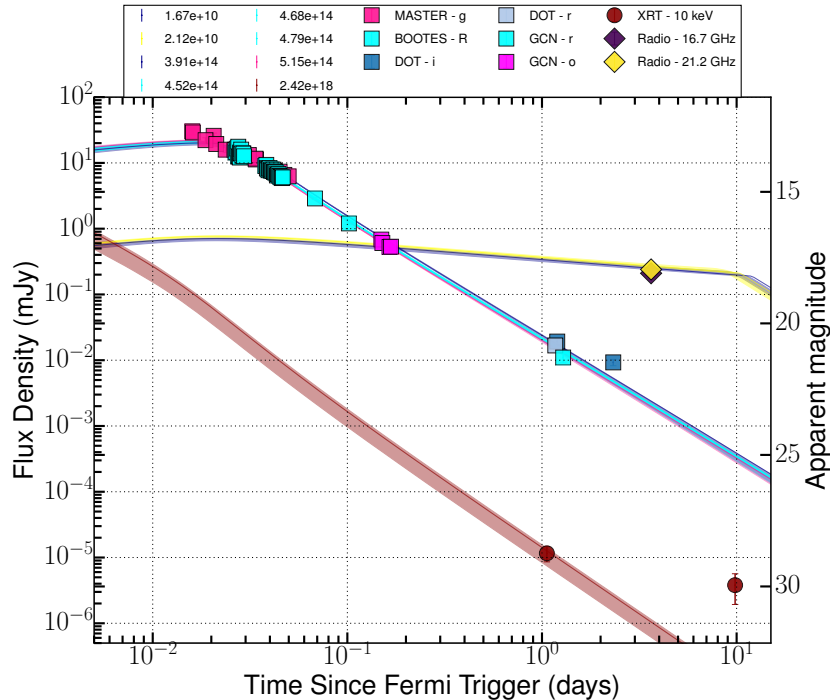


Figure 6. Broadband composite afterglow light curve of GRB 230204B, encompassing data from radio, optical, and X-ray observations. The light curve is modeled using a simple top-hat forward shock jet model in a homogeneous interstellar medium (ISM). The best-fit model, shown as solid lines, provides a good representation of the observed multi-wavelength data. The last XRT data point (close to the limit of the instrument), observed ~ 10 days post-burst, shows a deviation from the model prediction.

Self-Compton (SSC) contribution to afterglow, particularly at higher frequencies (Joshi & Razzaque 2021). However, in the case of GRB 230204B, the SSC effects appear negligible within the observed wavelength range (i.e., low-frequencies radio and optical), consistent with findings for similar GRBs (Gupta et al. 2022a; Wang et al. 2024). This is further supported by the temporal decay slopes, afterglow modeling (afterglowpy primarily models synchrotron emission processes), and lack of GeV emission (consistent with synchrotron-dominated regimes). Future studies focusing on a broader sample of bright GRBs with low ϵ_B , combined with well-sampled broadband light curves (from gamma-ray to radio) and afterglow modeling that includes SSC contributions, have the potential to shed light on their physical origins and diverse emission mechanisms.

4. DISCUSSION

4.1. Spectral evolution and Possible Radiation Mechanism

The spectral evolution of the prompt emission reveals complex temporal and spectral variability, which provides crucial insights into the nature of the emission mechanisms and the physical conditions in the GRB jet (Bošnjak & Daigne 2014). Typically, GRB prompt spec-

tra evolve over time, with the peak energy often shifting to lower energies as the burst progresses. This trend, known as “hard-to-soft” evolution, is commonly observed and is thought to reflect cooling processes within the jet (Norris et al. 1986; Bhat et al. 1994). Alternatively, “tracking” behavior, where E_p follows the intensity variations of the burst, has also been observed in some cases (Ryde & Svensson 1999), suggesting a possible relationship between the central engine activity and the observed emission (Gupta et al. 2021b).

The radiation mechanisms driving GRBs are fundamentally linked to the spectral index observed during the prompt emission phase and the overall radiative efficiency. The spectral index α_{pt} , which describes the shape of the GRB’s spectrum, provides crucial insights into the underlying physical processes. A harder low energy spectral index (i.e., closer to or exceeding $-2/3$) typically suggests a dominant photospheric or thermal component, where radiation emerges directly from the photosphere of the relativistic outflow. In contrast, a softer ($< -2/3$) often points to non-thermal processes, such as synchrotron emission, where electrons are accelerated in magnetic fields, producing a broad power-law spectrum (Chattopadhyay et al. 2022; Caballero-García et al. 2023).

To investigate the spectral evolution of GRB 230204B, we conducted a time-resolved spectral analysis, selecting time bins based on a Bayesian algorithm for optimal selection. The top panel of Figure 7 presents the deviation information criterion (DIC) values, comparing the **Band** function with the CPL for each time-resolved bin. The DIC comparison indicates that the majority of bins—excluding three—are better described by the traditional **Band** model. In the bottom panel of Figure 7, we illustrate the temporal evolution of key spectral parameters, including E_p , and α_{pt} , as derived from the **Band** and CPL models for GRB 230204B (see Table A1). These parameters are overlaid on the count-rate light curve of the burst’s prompt emission, revealing that the observed E_p exhibits an intensity-tracking behavior. Harder spectral indices during the first and second episodes might suggest a prominent photospheric component, which often produces harder spectra due to thermal-like emission (Ryde et al. 2010). The softer spectral indices during the later bins of the second, third, and fourth episodes might suggest a synchrotron-like emission becomes more prevalent in later times, indicating the coexistence of multiple emission mechanisms as the burst evolves (Li et al. 2021; Acuner & Ryde 2018).

Additionally, we explored correlations among the spectral parameters, examining (a) $\log(\text{Flux})$ versus $\log(E_p)$, (b) $\log(\text{Flux})$ versus α_{pt} , and (c) $\log(E_p)$ versus α_{pt} . Pearson correlation analysis was used to quantify the correlation strengths (Pearson correlation coefficient, r) and to assess the statistical significance (p -value) for each parameter pair. We noted a strong correlation for $\log(\text{Flux})$ versus $\log(E_p)$ of **Band** and CPL models with correlation coefficients equal to 0.69 and 0.73, respectively. We also noted a moderate correlation for $\log(\text{Flux})$ versus α_{pt} of **Band** model with a correlation coefficient equal to 0.46, but no correlation for $\log(E_p)$ versus α_{pt} .

The radiation efficiency of GRBs is another key factor, reflecting the fraction of the jet’s kinetic energy converted into gamma rays. It varies significantly depending on the dominant radiation mechanisms within the jet (Wang et al. 2015). In the photospheric model, radiation is produced as photons escape from the optically thick inner regions of the relativistic outflow. Energy is released at the photosphere where the flow becomes transparent, leading to thermal emission. Photospheric models tend to predict higher radiation efficiencies, sometimes exceeding 50-60%, especially if energy dissipation occurs near the photosphere (Lazzati et al. 2009; Beloborodov 2010; Pe’er & Ryde 2011; Lazzati et al. 2013). In contrast, the synchrotron models (arising from accelerated particles in internal shocks or magnetic reconnect-

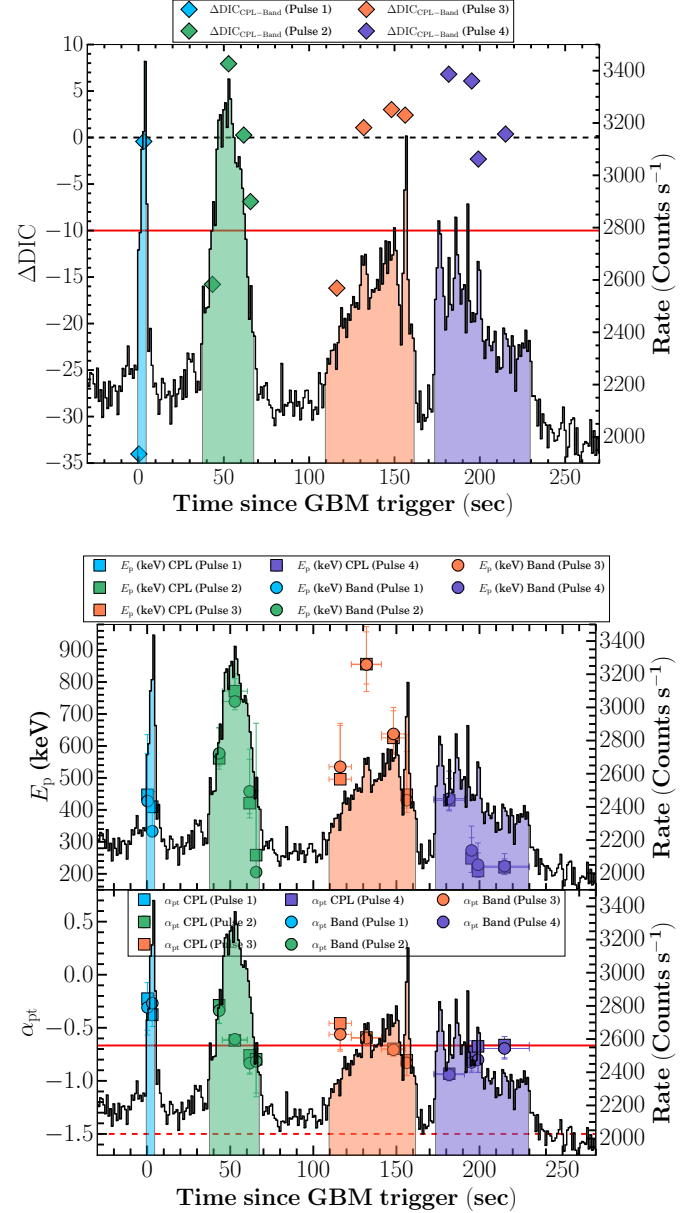


Figure 7. Top panel: The comparison between both phenomenological models using DIC values for individual time-bins. Bottom panel: Spectral evolution of GRB 230204B during prompt emission detected by *Fermi* GBM and derived from time-resolved spectral analysis. Variation of the peak energy during each episode of GRB 230204B. Changes in the low-energy spectral index, with horizontal dashed and dash-dotted lines representing the synchrotron “line of death” ($\alpha_{pt} = -2/3$) and the fast-cooling synchrotron limit ($\alpha_{pt} = -3/2$), respectively.

tion sites) often predict lower efficiencies, typically in the range of a few percent to 30%, in such cases much of the energy remains in the kinetic form rather than being radiated away (Kobayashi et al. 1997; Spada et al. 2000;

Beniamini & Piran 2013; Kumar & Zhang 2015). The hybrid model combines thermal photospheric emission with non-thermal synchrotron radiation from shocks or magnetic reconnections within the jet. This model can accommodate both thermal and non-thermal features in GRB spectra. Hybrid models can achieve efficiencies ranging from a few percent to 50% or higher, as they leverage both thermal and non-thermal emission processes (Zhang & Yan 2011; Zhang & Pe’er 2009; Vurm et al. 2011). These discussions suggest that GRBs may involve a complex interplay of thermal and non-thermal processes, with the relative contributions of these mechanisms varying across different bursts and even between different phases of the same burst.

The prompt emission and afterglow observations of GRB 230204B present intriguing insights into its jet structure and radiation mechanisms. Our analysis of the prompt emission reveals a spectral hardening during the initial pulses, with a subsequent softening in later pulses, consistent with a hybrid composition (baryonic + Poynting-flux) of Band + Blackbody components. This spectral evolution suggests that the jet may consist of both photospheric (thermal) and synchrotron (non-thermal) components, with the harder spectrum at the start dominated by a photospheric component and later phases increasingly influenced by synchrotron radiation (Sharma et al. 2020; Gupta et al. 2024c). Additionally, our afterglow modeling indicates a low gamma-ray efficiency of 4.3%, suggesting that most of the jet’s energy remains in kinetic form with minimal conversion into prompt gamma-ray emission. While the low gamma-ray efficiency supports a hybrid model, where both thermal photospheric and non-thermal synchrotron components coexist, it does not entirely rule out a synchrotron-only scenario (Rossi et al. 2002). Such a model, without any photospheric thermal emission, could also account for the low efficiency, provided the energy dissipation mechanism predominantly drives non-thermal radiation. However, the observed spectral evolution, with the initial hard component transitioning to softer emission, is more naturally explained by the presence of a photospheric contribution early on. Furthermore, the low gamma-ray efficiency aligns well with the characteristics of an ISM-like top-hat jet structure in the afterglow phase. In such a scenario, a top-hat jet interacting with a homogeneous interstellar medium produces a relatively uniform energy distribution across the jet, reducing the likelihood of highly efficient gamma-ray emission (Sari et al. 1998; Granot & Sari 2002; Zhang & Kobayashi 2005). This jet structure also favors an afterglow powered predominantly by forward shock emission, which is

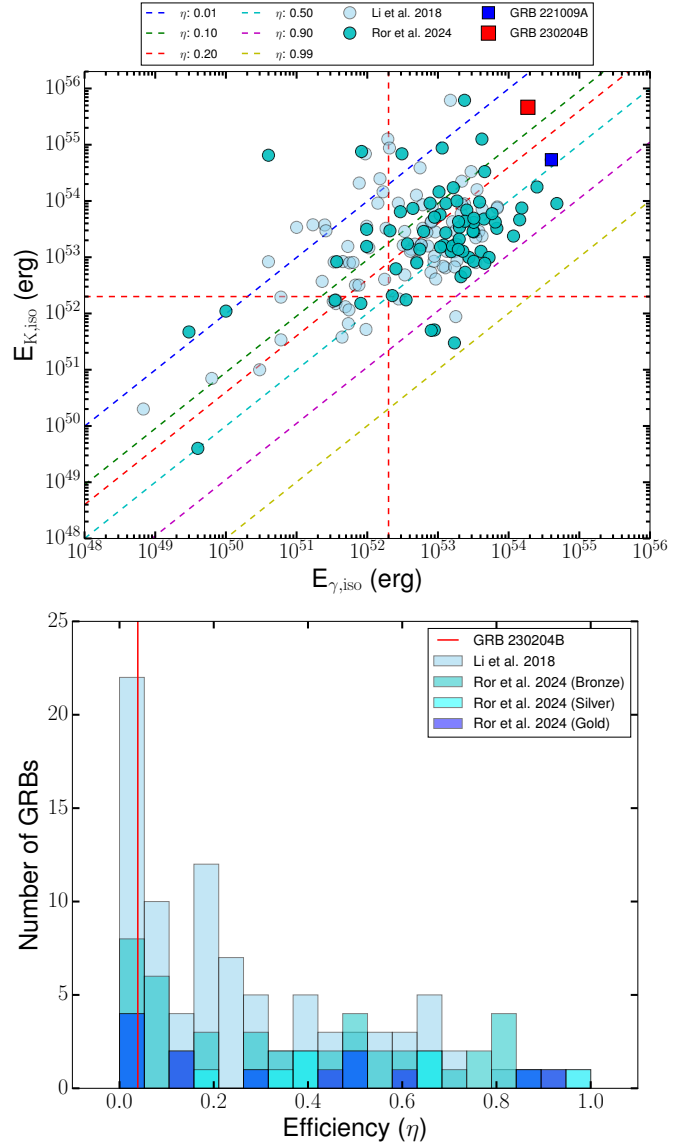


Figure 8. Top: Correlation between the isotropic-equivalent gamma-ray energy ($E_{\gamma,\text{iso}}$) and kinetic energy ($E_{K,\text{iso}}$, obtained from afterglow modeling) for GRB 230204B, compared to the broader GRB population obtained from Li et al. (2018); Ror et al. (2024). GRB 230204B is marked by a red square, indicating its position as a low-efficiency burst. The dashed lines represent the one-to-one correspondence between $E_{\gamma,\text{iso}}$ and $E_{K,\text{iso}}$. Bottom: Distribution of radiation efficiencies for a sample of GRBs, with GRB 230204B highlighted in red. The figure demonstrates the broad range of efficiencies across the population, with GRB 230204B residing in the low-efficiency tail. The red dashed lines correspond to the magnetar limit.

consistent with the observed light curve and its steady decay pattern.

The kinetic energy and $E_{\gamma,\text{iso}}$ of GRB 230204B place it within the population of GRBs characterized by rel-

atively low radiation efficiency. The kinetic energy for GRB 230204B, inferred from afterglow modeling, was found to be significantly higher than the isotropic gamma-ray energy, emphasizing that a substantial fraction of the jet’s energy remained in kinetic form and was not radiated as gamma rays. We noted that GRB 230204B has a higher $E_{K,iso}$ and $E_{\gamma,iso}$ values than expected from magnetar central engine (2×10^{52} erg, Metzger et al. 2011). This supports the rapidly rotating black hole as a possible central engine for this energetic and bright burst (Li et al. 2018; Ror et al. 2024). The distribution of radiation efficiencies across the GRB population, as shown in Figure 8, highlights GRB 230204B as the upper edge with a very low efficiency.

4.2. Brightness Comparison to GRB sample and physical scenarios for GRB 230204B

The optical luminosity of GRB 230204B (R/r-band and g-band data) has been compared with the population of GRBs with measured redshifts (Dainotti et al. 2024), providing valuable insights into its optical emission characteristics. The temporal evolution of GRB 230204B’s optical luminosity (see Figure 9) reveals an exceptionally bright initial emission, followed by a decay phase consistent with a forward shock model in a homogeneous interstellar medium (ISM). This places it among the brightest optical GRBs ever observed at the epoch of its detection, making it a standout event in the context of optical afterglow studies. The extreme optical brightness is an order of magnitude higher than other highly energetic bursts (~ 1.3 ks post-burst) such as GRB 080319B (Racusin et al. 2008; Pandey et al. 2009), GRB 990123 (Castro-Tirado et al. 1999), GRB 190114C (Misra et al. 2021; Gupta et al. 2021a), and GRB 221009A. Furthermore, we have also examined the optical luminosity of GRB 230204B at the epoch of its detection as a function of redshift for a population of GRBs with measured redshifts (Dainotti et al. 2024). We noted that GRB 230204B has the highest optical luminosity (~ 1.1 - 2.4 ks post-burst) with respect to all known GRBs with measured redshifts at the same epoch (see Figure 9). This suggests that GRB 230204B could represent a highly efficient energy transfer to the optical afterglow, or it might be related to the properties of its surrounding environment, jet structure, or progenitor system, contributing to its extraordinary luminosity.

Additionally, we noted that GRB 230204B follows an anti-correlation between the optical decay index and optical luminosity (Oates et al. 2012, 2015). There are several scenarios where such a correlation could be explained. Continued energy injection from a central engine, such as a magnetar or a rapidly spinning black hole,

could initially produce a very bright afterglow (Zhang & Mészáros 2001). However, if the injection is short-lived or if the engine rapidly loses power, the afterglow could exhibit a steep decay as the additional energy source wanes (Zhang & Mészáros 2001; Dai & Lu 1998). Our afterglow analysis did not show evidence of central engine activity (flare, plateau, variability, etc). A reverse shock could also produce a very luminous optical flash (Zhang & Kobayashi 2005). If the reverse shock is strong, it can dominate the early afterglow. Once the reverse shock fades, the light curve might steepen significantly, leading to a rapid decay. For GRB 230204B, however, our afterglow modeling suggests that a forward shock model could explain the early optical emission. Another possibility involves a structured jet, where a bright core with steep wings might cause a steep decay if the emission transitions from being core-dominated to wing-dominated, or if there is a slight change in the viewing angle (Rossi et al. 2002; Granot & Kumar 2003). However, our afterglow modeling suggests that a top-hat jet could explain the afterglow of GRB 230204B, so we discarded the structured jet for this burst. If the GRB is in a wind-like medium (density $\sim r^{-2}$), the early afterglow can be very bright (Chevalier & Li 2000). A change in the density profile (e.g., transition to a uniform medium) could cause the afterglow to decay steeply (Panaitescu & Kumar 2002; Starling et al. 2008). However, for GRB 230204B, our afterglow modeling suggests that an ISM-like medium could explain the broadband emission. A jet break occurs when the relativistic beaming angle of the jet becomes wider than the observer’s line of sight (Racusin et al. 2009). This typically results in a steepening of the afterglow light curve (Liang et al. 2008). An achromatic temporal slope of ~ -2 at late times could indicate that the break occurred, however, for GRB 230204B, synchronous broadband data is not available to confirm such behavior, also such an early jet break is not expected so we discarded the possibility. GRB afterglows depend strongly on the observer’s viewing angle relative to the jet’s core (Granot et al. 1999; van Eerten & MacFadyen 2013). When an observer views the GRB slightly off-axis but still close to the jet core, the observed afterglow appears very bright initially. This is due to the deceleration of the relativistic jet as it interacts with the surrounding medium, causing the beamed emission to broaden and spread into the observer’s line of sight. As the jet slows further and its emission becomes more isotropic, the light curve steepens, showing a rapid decline (Ryan et al. 2015). Such behavior suggests that GRB 230204B is observed close to the jet axis, as indicated by its narrow inferred viewing angle from afterglow modeling. The steep early optical

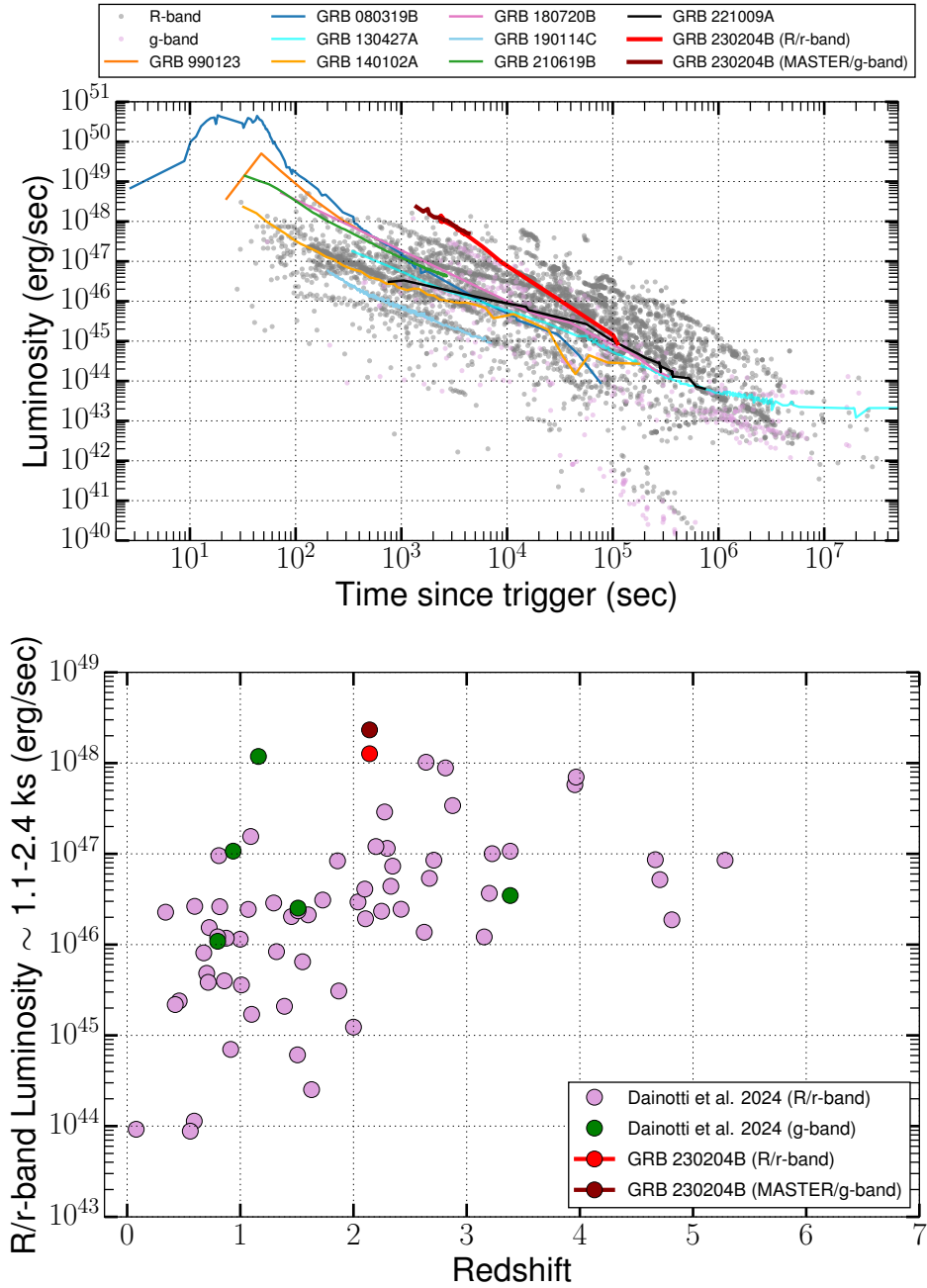


Figure 9. Top panel: Temporal evolution of the optical luminosity of GRB 230204B compared with a complete sample of well-studied GRBs with measured redshifts (Dainotti et al. 2024). The red solid curve represents the optical light curve of GRB 230204B, and the points show data from a sample of well-studied GRBs with measured redshifts. The comparison highlights the early extremely luminous optical emission and the subsequent decay phase of GRB 230204B, positioning it among the most luminous optical GRBs detected to date. Specific GRBs, such as GRB 990123, GRB 080319B, GRB 130427A, GRB 140102A, GRB 180720B, GRB 190114C, GRB 210619B, and GRB 221009A, are highlighted with individual lines as they represent notable cases with exceptionally bright afterglows. Bottom panel: Distribution of GRBs with measured redshifts as a function of optical luminosity at the epoch of the first optical detection of GRB 230204B. GRB 230204B is marked in red, showcasing its relative optical brightness within the broader GRB population. This figure indicates that GRB 230204B is the most luminous burst at the epoch of its first detection.

decay and extreme luminosity support this interpretation.

In Figure A3, we present a comparative analysis of the X-ray luminosity light curves of GRB 230204B with a sample of other GRBs that have measured redshifts (Gupta et al. 2024b). The X-ray flux data for these GRBs were sourced from the Swift XRT light curve repository⁴. To enable a direct comparison, the light curves are presented in the rest frame in the k-corrected co-moving bandpass, allowing for a consistent examination of intrinsic luminosity evolution across the sample. GRB 230204B is characterized by limited data, with only two available data points recorded at a late epoch, depicted in red on the plot. Despite the scarcity of data, the observed luminosity for GRB 230204B during this late phase is notably consistent with the average luminosity values observed in the comparative GRB sample at a similar epoch. This suggests that GRB 230204B’s X-ray luminosity profile falls within the expected range for GRBs in this phase.

In our analysis, we also examined the radio luminosity of GRB 230204B in the context of a broader sample of GRBs with known redshifts, as compiled by Shilling et al. (in preparation). Figure A3 illustrates the rest-frame 8.5 GHz luminosity light curves for this GRB sample, restricted to measurements with a signal-to-noise ratio (SNR) greater than 2 for clarity. For GRB 230204B specifically, we used a 9 GHz observation from ATCA as a close approximation to the 8.5 GHz rest-frame frequency. This 9 GHz upper limit, taken several days post-burst, is plotted alongside the 8.5 GHz light curve distribution. We noted that GRB 230204B’s radio upper limit appears on the higher side of the observed luminosity range for GRBs in the sample. The positioning of GRB 230204B’s radio data within this distribution provides valuable context for its radio emission profile relative to the larger GRB population. This comparison indicates that GRB 230204B’s intrinsic radio luminosity is consistent with the broader sample, suggesting it shares similar radio emission characteristics with typical GRBs.

5. SUMMARY

In this study, we conducted a comprehensive analysis of GRB 230204B, a long GRB observed across multiple wavelengths. Our observational campaign utilized both space-based telescopes, including *Fermi* GBM, MAXI, *Swift*/BAT, *Swift*/XRT, and *Swift*/UVOT, as well as ground-based observatories like BOOTES, MASTER,

DOT, and ATCA. The burst displayed a multi-pulse structure (each separated by periods of quiescence) with significant spectral variability, which we explored using time-resolved and time-integrated spectral analyses. Our findings indicate that the **Band** function, when combined with a **Blackbody** component, provided the best fit to the time-integrated spectra (indicating a potential mix of photospheric and synchrotron emission mechanisms), with variations in the preferred models across individual pulses. Furthermore, the time-resolved analysis reveals that the initial pulses of the prompt emission show harder spectra, while subsequent pulses become progressively softer, indicative of a hybrid jet composition.

Furthermore, the afterglow data collected across radio, optical, and X-ray wavelengths showed that GRB 230204B’s luminosity at various stages aligns with typical long-duration GRBs. Optical follow-up using multiple ground-based observatories revealed a rapid, early afterglow decay rate, which was more luminous than most GRBs at a similar epoch. Its high optical luminosity and bright afterglow suggest efficient energy transfer from the burst to the surrounding medium, or an environment conducive to high luminosity, possibly due to a structured jet.

Broadband afterglow modeling was conducted to investigate the GRB’s jet structure and surrounding environment. Using **afterglowpy/Redback**, we evaluated different jet profiles, concluding that a Top-Hat jet model best describes the data, with the inferred viewing and core angles suggesting a narrow, well-collimated jet structure. GRB 230204B exhibits an exceptionally high optical luminosity and an early steep optical decay, consistent with an observer viewing the burst nearly on-axis, as supported by afterglow modeling and a narrow inferred viewing angle. Our afterglow modeling supports a forward shock emission in a homogeneous interstellar medium (ISM), with no evidence of central engine activity. The optical luminosity and temporal decay index were found to align with existing GRB luminosity-decay correlations, further supporting a forward-shock-dominated afterglow. The radiative efficiency derived for GRB 230204B is lower (4.3%) compared to estimates reported for typical GRBs. The lower efficiency is primarily due to a lower magnetic field energy fraction, which leads to systematically higher estimates of $E_{K,iso}$. Consequently, this significantly mitigates the long-standing issue of low efficiency associated with internal shock models. We noted that GRB 230204B has a higher $E_{K,iso}$ and $E_{\gamma,iso}$ values than expected from magnetar central engine (2×10^{52} erg). This supports the

⁴ <https://www.swift.ac.uk>

rapidly rotating black hole as a possible central engine for this energetic and bright burst.

In summary, GRB 230204B's low gamma-ray efficiency and hybrid jet composition suggest a radiation mechanism where photospheric and synchrotron processes co-exist within the jet, influencing the spectral evolution of the prompt emission. This case highlights how the efficiency of GRB emissions depends not only on the jet composition and radiation processes but also on the structure of the jet and its interaction with the surrounding environment. Further studies of GRBs with similar spectral evolution and energy efficiency will help clarify the diversity of radiation mechanisms in GRBs and their implications for jet physics and energy dissipation.

Overall, our analysis of GRB 230204B underscores its importance as a reference for studying the emission mechanisms, jet structures, and afterglow behaviors of long-duration GRBs. The findings contribute to the growing understanding of GRB diversity and emphasize the role of broadband follow-up observations in exploring the complex evolution of these powerful cosmic events. Future studies of similar events, using well-coordinated observations across the spectrum, will be crucial in further refining our understanding of GRB physics and jet composition.

1 RG was sponsored by the National Aeronautics and
 2 Space Administration (NASA) through a contract with
 3 ORAU. The views and conclusions contained in this
 4 document are those of the authors and should not
 5 be interpreted as representing the official policies,
 6 either expressed or implied, of the National Aero-
 7 nautics and Space Administration (NASA) or the
 8 U.S. Government. The U.S. Government is autho-
 9 rized to reproduce and distribute reprints for Gov-
 10 ernment purposes notwithstanding any copyright no-
 11 tation herein. RG and SBP acknowledge the finan-
 12 cial support of ISRO under AstroSat archival Data
 13 utilization program (DS_2B-13013(2)/1/2021-Sec.2).
 14 RG, AKR, SBP, and AA acknowledge the BRICS
 15 grant DST/ICD/BRICS/Call5/CoNMuTraMO/2023
 16 (G) funded by the DST, India. This research has used
 17 data obtained through the HEASARC Online Service,
 18 provided by the NASA-GSFC, in support of NASA High
 19 Energy Astrophysics Programs. AA also acknowledges
 20 the Yushan Young Fellow Program by the Ministry
 21 of Education, Taiwan, for financial support. This work
 22 made use of data supplied by the UK Swift Science Data
 23 Centre at the University of Leicester. This research is
 24 based on observations obtained at the 3.6m Devasthal
 25 Optical Telescope (DOT), which is a National Facility
 26 run and managed by Aryabhata Research Institute of
 27 Observational Sciences (ARIES), an autonomous Insti-
 28 tute under the Department of Science and Technology,
 29 Government of India. The Australia Telescope Com-
 30 pact Array is part of the Australia Telescope National
 31 Facility (<https://ror.org/05qajvd42>) which is funded
 32 by the Australian Government for operation as a Na-
 33 tional Facility managed by CSIRO. We acknowledge
 34 the Gomeri people as the Traditional Owners of the
 35 Observatory site. Parts of this research were conducted
 36 with support from the Australian Research Council
 37 Centre of Excellence for Gravitational Wave Discovery
 38 (OzGrav), project number CE230100016. AJCT ac-
 39 knowledges support from the Spanish Ministry projects
 40 PID2020-118491GB-I00 and PID2023-151905OB-I00
 41 and Junta de Andalucía grant P20_010168 and from
 42 the Severo Ochoa grant CEX2021-001131-S funded by
 43 MCIN/AEI/10.13039/501100011033. SS acknowledges
 44 support from an STFC PhD studentship, the Faculty
 45 of Science and Technology at Lancaster University, and
 46 NASA under award number 80GSFC21M0002. MG ac-
 47 knowledges the Academy of Finland project no. 325806.
 48 The program of development within Priority-2030 is
 49 acknowledged for supporting the research at UrFU
 50 (04.89).

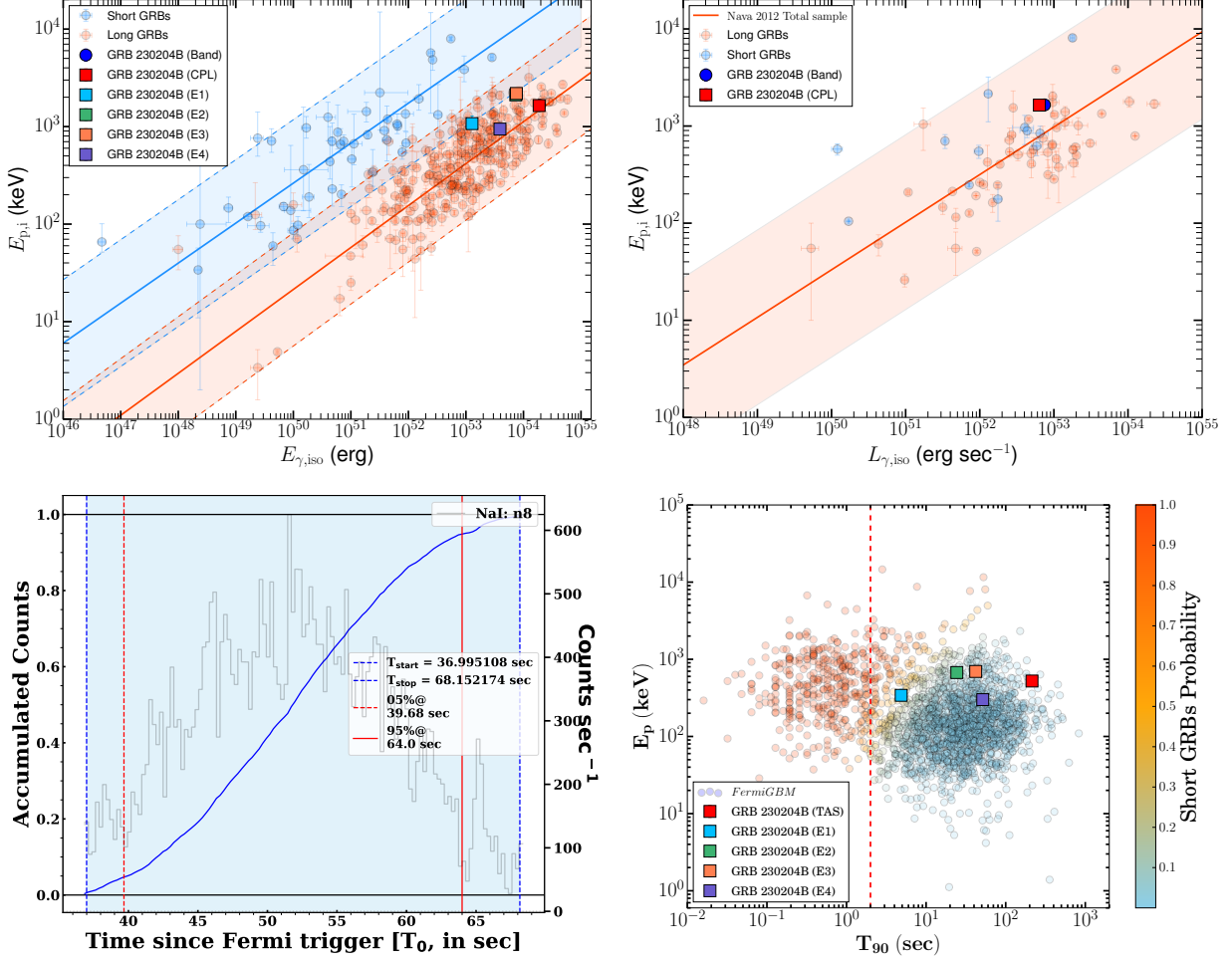


Figure A1. Top left: Pulse-wise Amati correlation for GRB 230204B. The position of individual pulses from GRB 230204B within the Amati correlation. Long and short gamma-ray bursts, as extensively analyzed in [Minaev & Pozanenko \(2020\)](#), are represented by orange and blue circles, respectively, with corresponding solid lines indicating linear fits for these groups. The shaded regions surrounding the lines illustrate the 3σ uncertainty bands. Top right: The placement of GRB 230204B on the Yonetoku correlation. Comparative positions of well-studied long and short bursts from [Nava et al. \(2012\)](#) are marked by blue and orange circles, with parallel shaded bands signifying the 3σ range. Colored squares denote the location of GRB 230204B pulses within each correlation framework. Bottom left: T_{90} calculation (accumulated counts as a function of time since T_0) for the second pulse of GRB 230204B. Bottom right: The pulse wise E_p - T_{90} plane for GRB 230204B and compare with a larger dataset of GRBs detected by the *Fermi* GBM.

Facilities: Fermi, MAXI, Swift, MASTER, BOOTES, DOT, ATCA

Software: astropy ([Astropy Collaboration et al. 2013, 2018](#)), Source Extractor ([Bertin & Arnouts 1996](#)), GBM-Tool ([Goldstein et al. 2022](#)), 3ML ([Vianello et al. 2015](#)), XSPEC ([Arnaud 1996](#)), DAOPHOT-II ([Stetson 1987](#)), IRAF ([Tody 1986, 1993](#)), Matplotlib ([Hunter 2007](#))

APPENDIX

A. FIGURES

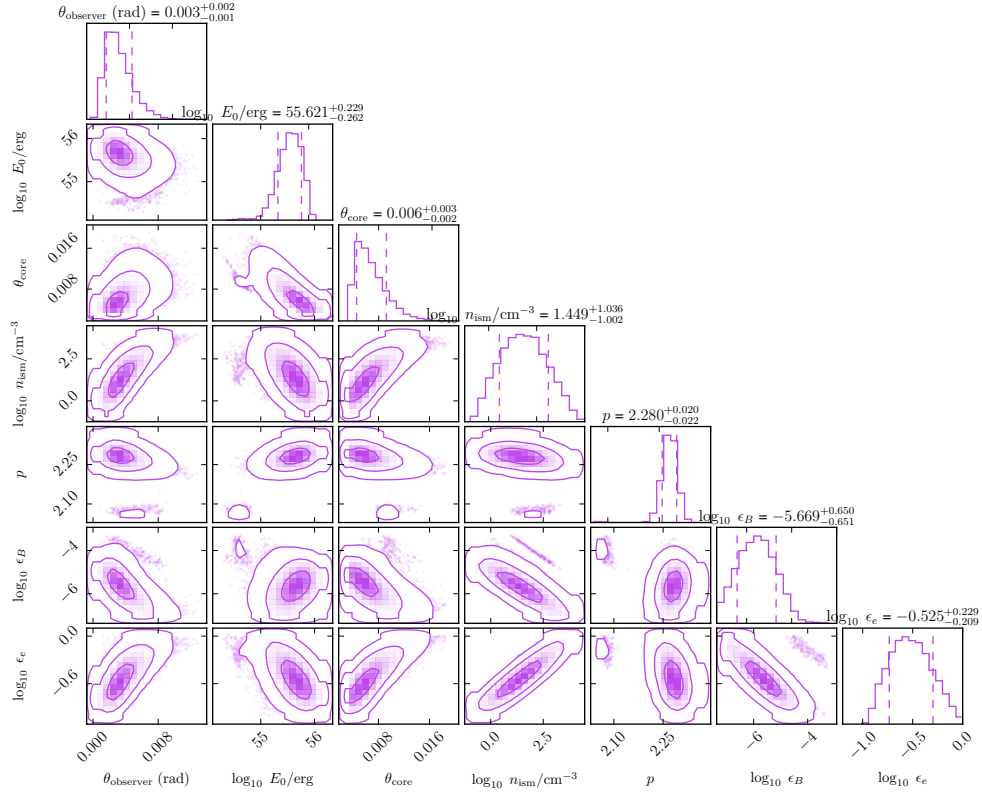


Figure A2. The corner plot presents the posterior distributions of the key afterglow model parameters, including jet opening angle, kinetic energy, and circumburst density. These distributions highlight the constraints derived from the broadband dataset and the robustness of the best-fit parameters.

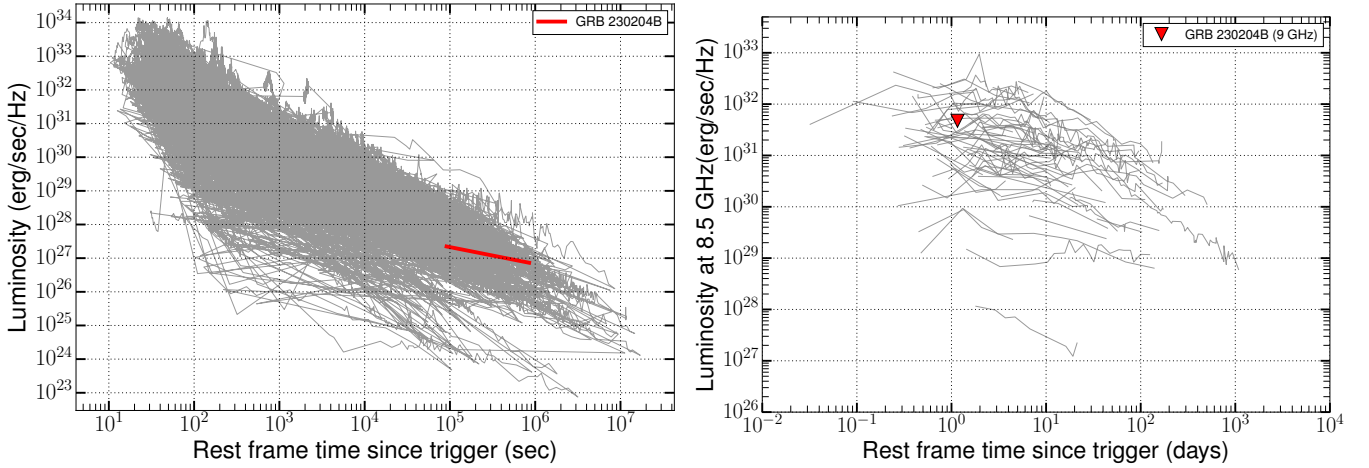


Figure A3. Left: X-ray luminosity light curves of GRB 230204B (in red) compared with other GRBs with known redshifts. The data were obtained from the *Swift*/XRT online repository (Evans et al. 2007, 2009). GRB 230204B’s light curve is limited to two late-time data points, indicating an average luminosity consistent with other GRBs at similar epochs. The comparison underscores the alignment of GRB 230204B’s late-phase luminosity with the general behavior observed in the broader GRB population. Right: Distribution of rest-frame 8.5 GHz radio luminosity light curves for a sample of GRBs with known redshifts (Shilling et al., in prep), where data points with SNR < 2 are excluded for clarity. For GRB 230204B, the 9 GHz upper limit observed with ATCA, taken several days post-burst, is overplotted for comparison, indicating a luminosity consistent with the general population. This placement highlights GRB 230204B’s relative position within the observed radio luminosity range of GRBs.

Table A1. Time-resolved spectral fitting results for the all emission episode of GRB 230204B, analyzed using the Band and CPL models. The table includes key spectral parameters such as the low-energy spectral index (α_{pt}), high-energy spectral index (β_{pt}) for the Band model, and the peak energy (E_p) for both models. Flux values (in erg), computed within the energy range of 8 keV to 40 MeV, are provided for each time bin.

T_{start} (sec)	T_{stop} (sec)	α_{pt}	β_{pt}	E_p (keV)	Flux $\times 10^{-06}$	DIC _{Band}	Γ_{CPL}	E_c (keV)	Flux $\times 10^{-06}$	DIC _{CPL}	Δ DIC
-0.8	1.234	$-0.31^{+0.23}_{-0.21}$	$-2.32^{+0.21}_{-1.99}$	$427.51^{+149.44}_{-81.48}$	1.6	2080.12	$-0.23^{+0.01}_{-0.34}$	$252.01^{+188.35}_{-0.63}$	1.31	2046.1	34.02
1.234	4.973	$-0.27^{+0.07}_{-0.17}$	$-2.21^{+0.09}_{-1.42}$	$333.22^{+87.52}_{-17.26}$	2.54	2812.46	$-0.38^{+0.05}_{-0.11}$	$252.35^{+47.30}_{-26.10}$	1.76	2812.03	0.43
41.412	45.259	$-0.34^{+0.10}_{-0.12}$	$-4.70^{+1.78}_{-0.06}$	$576.99^{+81.06}_{-49.44}$	1.93	2844.64	$-0.29^{+0.05}_{-0.17}$	$327.96^{+94.66}_{-24.04}$	1.78	2828.86	15.78
45.259	60.297	$-0.61^{+0.02}_{-0.05}$	$-2.70^{+0.12}_{-1.00}$	$739.04^{+71.32}_{-26.02}$	3.52	4361.92	$-0.62^{+0.03}_{-0.04}$	$558.51^{+54.45}_{-34.36}$	3.03	4369.86	-7.94
60.297	63.028	$-0.83^{+0.11}_{-0.10}$	$-3.28^{+0.86}_{-1.25}$	$458.05^{+100.28}_{-83.20}$	1.22	2501.94	$-0.76^{+0.04}_{-0.17}$	$339.72^{+168.87}_{-32.73}$	1.09	2502.2	-0.26
63.028	68.152	$-0.82^{+0.12}_{-0.30}$	$-1.86^{+0.03}_{-2.13}$	$205.43^{+254.66}_{-11.44}$	0.63	3138.76	$-0.80^{+0.01}_{-0.35}$	$214.89^{+12.66}_{-0.64}$	0.42	3131.87	6.89
109.451	122.927	$-0.56^{+0.10}_{-0.16}$	$-4.08^{+1.32}_{-0.52}$	$534.81^{+129.77}_{-52.64}$	0.71	4189.15	$-0.46^{+0.02}_{-0.25}$	$321.61^{+174.97}_{-10.84}$	0.64	4172.96	16.19
122.927	140.987	$-0.60^{+0.06}_{-0.06}$	$-3.49^{+0.58}_{-1.07}$	$854.61^{+102.21}_{-84.42}$	1.9	4522.29	$-0.59^{+0.05}_{-0.07}$	$607.82^{+17.27}_{-62.14}$	1.79	4523.35	-1.06
140.987	155.493	$-0.71^{+0.05}_{-0.06}$	$-4.50^{+1.42}_{-0.14}$	$637.62^{+72.21}_{-63.90}$	1.56	4261.59	$-0.70^{+0.04}_{-0.07}$	$480.27^{+95.07}_{-45.15}$	1.47	4264.6	-3.01
155.493	156.992	$-0.83^{+0.08}_{-0.12}$	$-2.45^{+0.07}_{-2.09}$	$430.08^{+152.15}_{-38.32}$	2.22	1898.35	$-0.81^{+0.04}_{-0.14}$	$374.93^{+188.57}_{-41.66}$	2.01	1900.76	-2.41
172.583	190.95	$-0.94^{+0.04}_{-0.06}$	$-4.51^{+1.52}_{-0.13}$	$435.13^{+63.33}_{-34.66}$	0.99	4436.83	$-0.93^{+0.03}_{-0.06}$	$403.22^{+91.05}_{-33.43}$	0.94	4443.64	-6.81
192.363	198.11	$-0.83^{+0.21}_{-0.08}$	$-4.86^{+2.50}_{-0.36}$	$273.23^{+39.77}_{-68.82}$	0.63	3236.22	$-0.73^{+0.04}_{-0.20}$	$195.33^{+100.71}_{-14.73}$	0.57	3242.3	-6.08
198.11	200.125	$-0.80^{+0.17}_{-0.12}$	$-4.21^{+1.40}_{-0.40}$	$228.30^{+37.12}_{-39.58}$	0.82	2116.74	$-0.67^{+0.03}_{-0.24}$	$157.75^{+87.55}_{-9.14}$	0.77	2114.43	2.31
200.125	230.0	$-0.69^{+0.11}_{-0.09}$	$-4.75^{+2.03}_{-0.18}$	$224.19^{+22.69}_{-26.60}$	0.39	4862.37	$-0.66^{+0.05}_{-0.13}$	$164.73^{+42.84}_{-13.22}$	0.37	4862.75	-0.38

Table A2. Log of X-ray afterglow observations of GRB 230204B. These data were obtained from the *Swift* XRT repository.

Time-T0 (sec)	Energy (keV)	FD (uJy)	FD Err	Telescope	Ref.
91528.12 ^{+18774.81} _{-10700.53}	10.0	0.0116	0.0030	XRT	This work
848730.52 ^{+17095.84} _{-7421.36}	10.0	0.0038	0.0019	XRT	This work

Table A3. Log of optical photometric observations of GRB 230204B.

Time-T0 (sec)	Filter	MAG (AB)	MAG Err	Telescope	Ref.
1378.42698	unfiltered	12.7	0.12	MASTER	This work
1777.40663	unfiltered	12.87	0.11	MASTER	This work
2930.5762	unfiltered	13.77	0.17	MASTER	This work
1389.55696	unfiltered	12.74	0.1	MASTER	This work
1611.76601	unfiltered	13.03	0.1	MASTER	This work
1830.95002	unfiltered	13.18	0.1	MASTER	This work
2048.95398	unfiltered	13.4	0.11	MASTER	This work
2267.91196	unfiltered	13.41	0.08	MASTER	This work
2486.30301	unfiltered	13.54	0.07	MASTER	This work
2694.05396	unfiltered	13.6	0.07	MASTER	This work
2914.54193	unfiltered	13.74	0.08	MASTER	This work
3654.57493	unfiltered	14.2	0.07	MASTER	This work
3877.80896	unfiltered	14.23	0.04	MASTER	This work
4097.35897	unfiltered	14.36	0.04	MASTER	This work
4316.58904	unfiltered	14.41	0.04	MASTER	This work
2296.5	clear	13.51	0.06	BOOTES	This work
2300.8	clear	13.4	0.29	BOOTES	This work
2319.4	clear	13.5	0.13	BOOTES	This work
2345.0	clear	13.37	0.13	BOOTES	This work
2363.8	clear	13.33	0.17	BOOTES	This work
2369.8	clear	13.65	0.16	BOOTES	This work
2375.9	clear	13.29	0.16	BOOTES	This work
2382.0	clear	13.66	0.14	BOOTES	This work
2399.4	clear	13.65	0.14	BOOTES	This work
2421.5	clear	13.7	0.15	BOOTES	This work
2427.6	clear	13.52	0.13	BOOTES	This work
2433.9	clear	13.5	0.11	BOOTES	This work
2439.9	clear	13.55	0.28	BOOTES	This work
2446.0	Clear	13.53	0.21	BOOTES	This work
2459.1	Clear	13.4	0.1	BOOTES	This work
2470.6	Clear	13.55	0.19	BOOTES	This work
2491.9	Clear	13.62	0.2	BOOTES	This work
2517.2	Clear	13.54	0.15	BOOTES	This work
2523.4	Clear	13.55	0.18	BOOTES	This work
2545.4	Clear	13.65	0.14	BOOTES	This work
3269.6	Clear	14.02	0.06	BOOTES	This work
3308.6	Clear	13.98	0.14	BOOTES	This work
3335.6	Clear	14.1	0.08	BOOTES	This work
3360.6	Clear	14.14	0.14	BOOTES	This work

Continued on next page

Time-T0 (sec)	Filter	MAG (AB)	MAG Err	Telescope	Ref.
3396.6	Clear	14.18	0.08	BOOTES	This work
3421.6	Clear	14.13	0.06	BOOTES	This work
3446.6	Clear	14.1	0.09	BOOTES	This work
3472.6	Clear	14.18	0.06	BOOTES	This work
3497.6	Clear	14.2	0.08	BOOTES	This work
3523.6	Clear	14.15	0.09	BOOTES	This work
3548.6	Clear	14.19	0.04	BOOTES	This work
3574.6	Clear	14.21	0.09	BOOTES	This work
3599.6	Clear	14.16	0.08	BOOTES	This work
3626.6	Clear	14.25	0.08	BOOTES	This work
3651.6	Clear	14.23	0.08	BOOTES	This work
3677.6	Clear	14.27	0.13	BOOTES	This work
3703.6	Clear	14.25	0.08	BOOTES	This work
3729.6	Clear	14.3	0.07	BOOTES	This work
3755.6	Clear	14.38	0.09	BOOTES	This work
3781.6	Clear	14.35	0.13	BOOTES	This work
3806.6	Clear	14.35	0.08	BOOTES	This work
3831.6	Clear	14.33	0.05	BOOTES	This work
3858.6	Clear	14.38	0.07	BOOTES	This work
3884.6	Clear	14.4	0.1	BOOTES	This work
3909.6	Clear	14.44	0.06	BOOTES	This work
3935.6	Clear	14.44	0.09	BOOTES	This work
3960.6	Clear	14.46	0.05	BOOTES	This work
3988.6	Clear	14.48	0.07	BOOTES	This work
4028.6	Clear	14.45	0.08	BOOTES	This work
101119.0	<i>r</i>	21.09	0.09	DOT	This work
278325.4	<i>r</i>	> 21.27	–	DOT	This work
103451.8	<i>i</i>	20.88	0.10	DOT	This work
200738.2	<i>i</i>	21.67	0.12	DOT	This work
105611.8	<i>g</i>	> 22.27	–	DOT	This work
95569.7	<i>V</i>	>18.94		UVOT	This work
95159.7	<i>B</i>	>19.50		UVOT	This work
95075.4	<i>U</i>	>20.57		UVOT	This work
93868.0	<i>UVW1</i>	>19.53		UVOT	This work
89647.6	<i>UVM2</i>	>21.7		UVOT	This work
89126.7	<i>UVW2</i>	>19.78		UVOT	This work
841905.2	<i>UVW2</i>	>20.81		UVOT	This work
5889.9	<i>r</i>	15.25	0.04	GIT	GCN
8801.5	<i>r</i>	16.20	0.05	GIT	GCN
12905.8	<i>o</i>	16.82	0.04	ATLAS	GCN
13064.8	<i>o</i>	16.95	0.05	ATLAS	GCN
14204.8	<i>o</i>	17.10	0.05	ATLAS	GCN
14477.8	<i>o</i>	17.09	0.05	ATLAS	GCN
110948.8	<i>r</i>	21.30	0.18	VLT	GCN

Table A4. Log of radio follow-up observations of GRB 230204B.

Time-T0 (sec)	Freq (GHz)	FD (mJy)	FD Err	Telescope	Ref.
314133	5.5	<0.45		ATCA	This work
314133	9.0	<0.20		ATCA	This work
314133	16.7	0.21	0.02	ATCA	This work
314133	21.2	0.24	0.05	ATCA	This work
314133	33.0	<0.12		ATCA	This work
314133	35.0	<0.13		ATCA	This work
12658049	0.842	<1.31		ASKAP	This work
28948293	0.943	<1.45		ASKAP	This work

Table A5. MAXI constrained (3σ) on the X-ray afterglow emission of GRB 230204B.

T-T ₀ (sec)	Energy range exposure	Upper limit (mJy)
22526	2-20 keV	0.052
28102	2-20 keV	0.042
33679	2-20 keV	0.047
39257	2-20 keV	0.047
44834	2-20 keV	0.058
50409	2-20 keV	0.062
55986	2-20 keV	0.058
61563	2-20 keV	0.057
67140	2-20 keV	0.053
72717	2-20 keV	0.055
78292	2-20 keV	0.055

REFERENCES

- Acuner, Z., & Ryde, F. 2018, *MNRAS*, 475, 1708, doi: [10.1093/mnras/stx3106](https://doi.org/10.1093/mnras/stx3106)
- Amati, L. 2006, *MNRAS*, 372, 233, doi: [10.1111/j.1365-2966.2006.10840.x](https://doi.org/10.1111/j.1365-2966.2006.10840.x)
- Arnaud, K. A. 1996, in *Astronomical Society of the Pacific Conference Series*, Vol. 101, *Astronomical Data Analysis Software and Systems V*, ed. G. H. Jacoby & J. Barnes, 17
- Astropy Collaboration, Robitaille, T. P., Tollerud, E. J., et al. 2013, *A&A*, 558, A33, doi: [10.1051/0004-6361/201322068](https://doi.org/10.1051/0004-6361/201322068)
- Astropy Collaboration, Price-Whelan, A. M., Sipőcz, B. M., et al. 2018, *AJ*, 156, 123, doi: [10.3847/1538-3881/aabc4f](https://doi.org/10.3847/1538-3881/aabc4f)
- Barthelmy, S. 2016, in *APS Meeting Abstracts*, Vol. 2016, *APS April Meeting Abstracts*, M13.004
- Barthelmy, S. D. 2003, in *American Astronomical Society Meeting Abstracts*, Vol. 202, *American Astronomical Society Meeting Abstracts #202*, 45.07
- Barthelmy, S. D., Butterworth, P., Cline, T. L., et al. 1998, in *American Institute of Physics Conference Series*, Vol. 428, *Gamma-Ray Bursts, 4th Huntsville Symposium*, ed. C. A. Meegan, R. D. Preece, & T. M. Koshut (AIP), 99–103, doi: [10.1063/1.55426](https://doi.org/10.1063/1.55426)
- Basak, R., & Rao, A. R. 2013, *MNRAS*, 436, 3082, doi: [10.1093/mnras/stt1790](https://doi.org/10.1093/mnras/stt1790)
- Beloborodov, A. M. 2010, *MNRAS*, 407, 1033, doi: [10.1111/j.1365-2966.2010.16770.x](https://doi.org/10.1111/j.1365-2966.2010.16770.x)
- Beniamini, P., & Piran, T. 2013, *ApJ*, 769, 69, doi: [10.1088/0004-637X/769/1/69](https://doi.org/10.1088/0004-637X/769/1/69)
- Bertin, E., & Arnouts, S. 1996, *A&AS*, 117, 393, doi: [10.1051/aas:1996164](https://doi.org/10.1051/aas:1996164)
- Bhat, P. N., Fishman, G. J., Meegan, C. A., et al. 1994, *ApJ*, 426, 604, doi: [10.1086/174097](https://doi.org/10.1086/174097)
- Bošnjak, Ž., & Daigne, F. 2014, *A&A*, 568, A45, doi: [10.1051/0004-6361/201322341](https://doi.org/10.1051/0004-6361/201322341)
- Breeveld, A. A., Landsman, W., Holland, S. T., et al. 2011, in *American Institute of Physics Conference Series*, Vol. 1358, *American Institute of Physics Conference Series*, ed. J. E. McEnery, J. L. Racusin, & N. Gehrels, 373–376, doi: [10.1063/1.3621807](https://doi.org/10.1063/1.3621807)

- Caballero-García, M. D., Gupta, R., Pandey, S. B., et al. 2023, *MNRAS*, 519, 3201, doi: [10.1093/mnras/stac3629](https://doi.org/10.1093/mnras/stac3629)
- Casentini, C., Pittori, C., Tavani, M., et al. 2023, *GRB Coordinates Network*, 33272, 1
- Castro-Tirado, A. J. 2023, *Nature Astronomy*, 7, 1136, doi: [10.1038/s41550-023-02075-w](https://doi.org/10.1038/s41550-023-02075-w)
- Castro-Tirado, A. J., Zapatero-Osorio, M. R., Caon, N., et al. 1999, *Science*, 283, 2069, doi: [10.1126/science.283.5410.2069](https://doi.org/10.1126/science.283.5410.2069)
- Castro-Tirado, A. J., Jelínek, M., Gorosabel, J., et al. 2012, in *Astronomical Society of India Conference Series*, Vol. 7, *Astronomical Society of India Conference Series*, 313–320
- Chand, V., Banerjee, A., Gupta, R., et al. 2020, *ApJ*, 898, 42, doi: [10.3847/1538-4357/ab9606](https://doi.org/10.3847/1538-4357/ab9606)
- Chattopadhyay, T., Gupta, S., Iyyani, S., et al. 2022, *ApJ*, 936, 12, doi: [10.3847/1538-4357/ac82ef](https://doi.org/10.3847/1538-4357/ac82ef)
- Chevalier, R. A., & Li, Z.-Y. 2000, *ApJ*, 536, 195, doi: [10.1086/308914](https://doi.org/10.1086/308914)
- Clark, B. G. 1980, *A&A*, 89, 377
- Condon, J. J., Cotton, W. D., Greisen, E. W., et al. 1998, *AJ*, 115, 1693, doi: [10.1086/300337](https://doi.org/10.1086/300337)
- Costa, E., Frontera, F., Heise, J., et al. 1997, *Nature*, 387, 783, doi: [10.1038/42885](https://doi.org/10.1038/42885)
- Dafcikova, M., Ripa, J., Pal, A., et al. 2023, *GRB Coordinates Network*, 33273, 1
- Dai, Z. G., & Lu, T. 1998, *A&A*, 333, L87, doi: [10.48550/arXiv.astro-ph/9810402](https://doi.org/10.48550/arXiv.astro-ph/9810402)
- Dainotti, M. G., Levine, D., Fraija, N., Warren, D., & Sourav, S. 2022, *ApJ*, 940, 169, doi: [10.3847/1538-4357/ac9b11](https://doi.org/10.3847/1538-4357/ac9b11)
- Dainotti, M. G., De Simone, B., Mohideen Malik, R. F., et al. 2024, *MNRAS*, 533, 4023, doi: [10.1093/mnras/stae1484](https://doi.org/10.1093/mnras/stae1484)
- D’Elia, V., Beardmore, A. P., D’Avanzo, P., et al. 2023, *GRB Coordinates Network*, 33285, 1
- Ershova, O. A., Lipunov, V. M., Gorbvskoy, E. S., et al. 2020, *Astronomy Reports*, 64, 126, doi: [10.1134/S1063772920020018](https://doi.org/10.1134/S1063772920020018)
- Evans, P. A., Beardmore, A. P., Page, K. L., et al. 2007, *A&A*, 469, 379, doi: [10.1051/0004-6361:20077530](https://doi.org/10.1051/0004-6361:20077530)
- . 2009, *MNRAS*, 397, 1177, doi: [10.1111/j.1365-2966.2009.14913.x](https://doi.org/10.1111/j.1365-2966.2009.14913.x)
- Fraija, N., Lee, W., & Veres, P. 2016, *ApJ*, 818, 190, doi: [10.3847/0004-637X/818/2/190](https://doi.org/10.3847/0004-637X/818/2/190)
- Frail, D. A., Kulkarni, S. R., Nicastro, L., Feroci, M., & Taylor, G. B. 1997, *Nature*, 389, 261, doi: [10.1038/38451](https://doi.org/10.1038/38451)
- Gehrels, N., Chincarini, G., Giommi, P., et al. 2004, *ApJ*, 611, 1005, doi: [10.1086/422091](https://doi.org/10.1086/422091)
- Goldstein, A., Cleveland, W. H., & Kocevski, D. 2022, *Fermi GBM Data Tools: v1.1.1*. <https://fermi.gsfc.nasa.gov/ssc/data/analysis/gbm>
- Granot, J., & Kumar, P. 2003, *ApJ*, 591, 1086, doi: [10.1086/375489](https://doi.org/10.1086/375489)
- Granot, J., Piran, T., & Sari, R. 1999, *ApJ*, 513, 679, doi: [10.1086/306884](https://doi.org/10.1086/306884)
- Granot, J., & Sari, R. 2002, *ApJ*, 568, 820, doi: [10.1086/338966](https://doi.org/10.1086/338966)
- Gupta, R. 2023, *arXiv e-prints*, arXiv:2312.16265, doi: [10.48550/arXiv.2312.16265](https://doi.org/10.48550/arXiv.2312.16265)
- Gupta, R., Bhushan Pandey, S., Ror, A. K., Aryan, A., & Nath Tiwari, S. 2024a, *Bulletin de la Societe Royale des Sciences de Liege*, 93, 683, doi: [10.25518/0037-9565.11838](https://doi.org/10.25518/0037-9565.11838)
- Gupta, R., Pandey, S. B., Castro-Tirado, A. J., et al. 2021a, in *Revista Mexicana de Astronomia y Astrofisica Conference Series*, Vol. 53, *Revista Mexicana de Astronomia y Astrofisica Conference Series*, 113–123, doi: [10.22201/ia.14052059p.2021.53.23](https://doi.org/10.22201/ia.14052059p.2021.53.23)
- Gupta, R., Ror, A. K., Pandey, S. B., et al. 2024b, *arXiv e-prints*, arXiv:2409.04871, doi: [10.48550/arXiv.2409.04871](https://doi.org/10.48550/arXiv.2409.04871)
- Gupta, R., Oates, S. R., Pandey, S. B., et al. 2021b, *MNRAS*, 505, 4086, doi: [10.1093/mnras/stab1573](https://doi.org/10.1093/mnras/stab1573)
- Gupta, R., Gupta, S., Chattopadhyay, T., et al. 2022a, *MNRAS*, 511, 1694, doi: [10.1093/mnras/stac015](https://doi.org/10.1093/mnras/stac015)
- Gupta, R., Pandey, S. B., Kumar, A., et al. 2022b, *Journal of Astrophysics and Astronomy*, 43, 82, doi: [10.1007/s12036-022-09865-0](https://doi.org/10.1007/s12036-022-09865-0)
- Gupta, R., Kumar, A., Pandey, S. B., et al. 2022c, *Journal of Astrophysics and Astronomy*, 43, 11, doi: [10.1007/s12036-021-09794-4](https://doi.org/10.1007/s12036-021-09794-4)
- Gupta, R., Pandey, S. B., Gupta, S., et al. 2024c, *ApJ*, 972, 166, doi: [10.3847/1538-4357/ad5a92](https://doi.org/10.3847/1538-4357/ad5a92)
- Hunter, J. D. 2007, *Computing in Science and Engineering*, 9, 90, doi: [10.1109/MCSE.2007.55](https://doi.org/10.1109/MCSE.2007.55)
- Jordana-Mitjans, N., Mundell, C. G., Kobayashi, S., et al. 2020, *ApJ*, 892, 97, doi: [10.3847/1538-4357/ab7248](https://doi.org/10.3847/1538-4357/ab7248)
- Joshi, J. C., & Razzaque, S. 2021, *MNRAS*, 505, 1718, doi: [10.1093/mnras/stab1329](https://doi.org/10.1093/mnras/stab1329)
- Kann, D. A., Klose, S., Zhang, B., et al. 2010, *ApJ*, 720, 1513, doi: [10.1088/0004-637X/720/2/1513](https://doi.org/10.1088/0004-637X/720/2/1513)
- Kennea, J. A., Raman, G., DeLaunay, J., & Tohuvavohu, A. 2023, *GRB Coordinates Network*, 33267, 1
- Kobayashi, S., Piran, T., & Sari, R. 1997, *ApJ*, 490, 92, doi: [10.1086/512791](https://doi.org/10.1086/512791)
- Kornilov, V. G., Lipunov, V. M., Gorbvskoy, E. S., et al. 2012, *Experimental Astronomy*, 33, 173, doi: [10.1007/s10686-011-9280-z](https://doi.org/10.1007/s10686-011-9280-z)

- Kouveliotou, C., Meegan, C. A., Fishman, G. J., et al. 1993, *ApJL*, 413, L101, doi: [10.1086/186969](https://doi.org/10.1086/186969)
- Kumar, P., & Barniol Duran, R. 2009, *MNRAS*, 400, L75, doi: [10.1111/j.1745-3933.2009.00766.x](https://doi.org/10.1111/j.1745-3933.2009.00766.x)
- . 2010, *MNRAS*, 409, 226, doi: [10.1111/j.1365-2966.2010.17274.x](https://doi.org/10.1111/j.1365-2966.2010.17274.x)
- Kumar, P., & Zhang, B. 2015, *PhR*, 561, 1, doi: [10.1016/j.physrep.2014.09.008](https://doi.org/10.1016/j.physrep.2014.09.008)
- Lacy, M., Baum, S. A., Chandler, C. J., et al. 2020, *PASP*, 132, 035001, doi: [10.1088/1538-3873/ab63eb](https://doi.org/10.1088/1538-3873/ab63eb)
- Lazzati, D., Morsony, B. J., & Begelman, M. C. 2009, *ApJL*, 700, L47, doi: [10.1088/0004-637X/700/1/L47](https://doi.org/10.1088/0004-637X/700/1/L47)
- Lazzati, D., Morsony, B. J., Margutti, R., & Begelman, M. C. 2013, *ApJ*, 765, 103, doi: [10.1088/0004-637X/765/2/103](https://doi.org/10.1088/0004-637X/765/2/103)
- Leung, J. K., Murphy, T., Ghirlanda, G., et al. 2021, *MNRAS*, 503, 1847, doi: [10.1093/mnras/stab326](https://doi.org/10.1093/mnras/stab326)
- Li, L., Ryde, F., Pe'er, A., Yu, H.-F., & Acuner, Z. 2021, *ApJS*, 254, 35, doi: [10.3847/1538-4365/abee2a](https://doi.org/10.3847/1538-4365/abee2a)
- Li, L., Wu, X.-F., Lei, W.-H., et al. 2018, *ApJS*, 236, 26, doi: [10.3847/1538-4365/aabaf3](https://doi.org/10.3847/1538-4365/aabaf3)
- Li, L., Liang, E.-W., Tang, Q.-W., et al. 2012, *ApJ*, 758, 27, doi: [10.1088/0004-637X/758/1/27](https://doi.org/10.1088/0004-637X/758/1/27)
- Liang, E.-W., Racusin, J. L., Zhang, B., Zhang, B.-B., & Burrows, D. N. 2008, *ApJ*, 675, 528, doi: [10.1086/524701](https://doi.org/10.1086/524701)
- Liang, E.-W., Yi, S.-X., Zhang, J., et al. 2010, *ApJ*, 725, 2209, doi: [10.1088/0004-637X/725/2/2209](https://doi.org/10.1088/0004-637X/725/2/2209)
- Lipunov, V., Kornilov, V., Gorbvskoy, E., et al. 2010a, *Advances in Astronomy*, 2010, 349171, doi: [10.1155/2010/349171](https://doi.org/10.1155/2010/349171)
- . 2010b, *Advances in Astronomy*, 2010, 349171, doi: [10.1155/2010/349171](https://doi.org/10.1155/2010/349171)
- Lipunov, V. M., Vladimirov, V. V., Gorbvskoi, E. S., et al. 2019, *Astronomy Reports*, 63, 293, doi: [10.1134/S1063772919040073](https://doi.org/10.1134/S1063772919040073)
- Lipunov, V. M., Kornilov, V. G., Zhirkov, K., et al. 2022, *Universe*, 8, 271, doi: [10.3390/universe8050271](https://doi.org/10.3390/universe8050271)
- Lipunov, V. M., Kornilov, V. G., Zhirkov, K. K., et al. 2023, *Astronomy Reports*, 67, S140, doi: [10.1134/S1063772923140123](https://doi.org/10.1134/S1063772923140123)
- Matsuoka, M., Kawasaki, K., Ueno, S., et al. 2009, *PASJ*, 61, 999. <https://arxiv.org/abs/0906.0631>
- Mauch, T., Murphy, T., Buttery, H. J., et al. 2003, *MNRAS*, 342, 1117, doi: [10.1046/j.1365-8711.2003.06605.x](https://doi.org/10.1046/j.1365-8711.2003.06605.x)
- McConnell, D., Hale, C. L., Lenc, E., et al. 2020, *PASA*, 37, e048, doi: [10.1017/pasa.2020.41](https://doi.org/10.1017/pasa.2020.41)
- Meszáros, P., & Rees, M. J. 1997a, *ApJ*, 476, 232, doi: [10.1086/303625](https://doi.org/10.1086/303625)
- . 1997b, 476, 232, doi: [10.1086/303625](https://doi.org/10.1086/303625)
- Metzger, B. D., Giannios, D., Thompson, T. A., Bucciantini, N., & Quataert, E. 2011, *MNRAS*, 413, 2031, doi: [10.1111/j.1365-2966.2011.18280.x](https://doi.org/10.1111/j.1365-2966.2011.18280.x)
- Minaev, P. Y., & Pozanenko, A. S. 2020, *MNRAS*, 492, 1919, doi: [10.1093/mnras/stz3611](https://doi.org/10.1093/mnras/stz3611)
- Misra, K., Resmi, L., Kann, D. A., et al. 2021, *MNRAS*, 504, 5685, doi: [10.1093/mnras/stab1050](https://doi.org/10.1093/mnras/stab1050)
- Nava, L., Salvaterra, R., Ghirlanda, G., et al. 2012, *MNRAS*, 421, 1256, doi: [10.1111/j.1365-2966.2011.20394.x](https://doi.org/10.1111/j.1365-2966.2011.20394.x)
- Negoro, H., Kohama, M., Serino, M., et al. 2016, *PASJ*, 68, S1, doi: [10.1093/pasj/psw016](https://doi.org/10.1093/pasj/psw016)
- Norris, J. P., Share, G. H., Messina, D. C., et al. 1986, *ApJ*, 301, 213, doi: [10.1086/163889](https://doi.org/10.1086/163889)
- Oates, S. R., Page, M. J., De Pasquale, M., et al. 2012, *MNRAS*, 426, L86, doi: [10.1111/j.1745-3933.2012.01331.x](https://doi.org/10.1111/j.1745-3933.2012.01331.x)
- Oates, S. R., Racusin, J. L., De Pasquale, M., et al. 2015, *MNRAS*, 453, 4121, doi: [10.1093/mnras/stv1956](https://doi.org/10.1093/mnras/stv1956)
- Panaitescu, A., & Kumar, P. 2002, *ApJ*, 571, 779, doi: [10.1086/340094](https://doi.org/10.1086/340094)
- Pandey, S. B. 2016, in *Revista Mexicana de Astronomía y Astrofísica Conference Series*, Vol. 48, *Revista Mexicana de Astronomía y Astrofísica Conference Series*, 83–88
- Pandey, S. B., Castro-Tirado, A. J., Jelínek, M., et al. 2009, *A&A*, 504, 45, doi: [10.1051/0004-6361/200811135](https://doi.org/10.1051/0004-6361/200811135)
- Parsotan, T., Laha, S., Palmer, D. M., et al. 2023, *ApJ*, 953, 155, doi: [10.3847/1538-4357/ace325](https://doi.org/10.3847/1538-4357/ace325)
- Pe'er, A., & Ryde, F. 2011, *ApJ*, 732, 49, doi: [10.1088/0004-637X/732/1/49](https://doi.org/10.1088/0004-637X/732/1/49)
- Piran, T. 1999, *PhR*, 314, 575, doi: [10.1016/S0370-1573\(98\)00127-6](https://doi.org/10.1016/S0370-1573(98)00127-6)
- Poolakkil, S., Meegan, C., & Fermi GBM Team. 2023, *GRB Coordinates Network*, 33288, 1
- Poole, T. S., Breeveld, A. A., Page, M. J., et al. 2008, 383, 627, doi: [10.1111/j.1365-2966.2007.12563.x](https://doi.org/10.1111/j.1365-2966.2007.12563.x)
- Racusin, J. L., Karpov, S. V., Sokolowski, M., et al. 2008, *Nature*, 455, 183, doi: [10.1038/nature07270](https://doi.org/10.1038/nature07270)
- Racusin, J. L., Liang, E. W., Burrows, D. N., et al. 2009, *ApJ*, 698, 43, doi: [10.1088/0004-637X/698/1/43](https://doi.org/10.1088/0004-637X/698/1/43)
- Ror, A. K., Ghosh, A., Kumar, B., et al. 2023a, *GRB Coordinates Network*, 33284, 1
- Ror, A. K., Gupta, R., Aryan, A., et al. 2024, *ApJ*, 971, 163, doi: [10.3847/1538-4357/ad5554](https://doi.org/10.3847/1538-4357/ad5554)
- Ror, A. K., Gupta, R., Jelínek, M., et al. 2023b, *ApJ*, 942, 34, doi: [10.3847/1538-4357/aca414](https://doi.org/10.3847/1538-4357/aca414)
- Rossi, E., Lazzati, D., & Rees, M. J. 2002, *MNRAS*, 332, 945, doi: [10.1046/j.1365-8711.2002.05363.x](https://doi.org/10.1046/j.1365-8711.2002.05363.x)
- Ryan, G., van Eerten, H., MacFadyen, A., & Zhang, B.-B. 2015, *ApJ*, 799, 3, doi: [10.1088/0004-637X/799/1/3](https://doi.org/10.1088/0004-637X/799/1/3)

- Ryan, G., van Eerten, H., Piro, L., & Troja, E. 2020, *ApJ*, 896, 166, doi: [10.3847/1538-4357/ab93cf](https://doi.org/10.3847/1538-4357/ab93cf)
- Ryde, F., & Svensson, R. 1999, *ApJ*, 512, 693, doi: [10.1086/306818](https://doi.org/10.1086/306818)
- Ryde, F., Axelsson, M., Zhang, B. B., et al. 2010, *ApJL*, 709, L172, doi: [10.1088/2041-8205/709/2/L172](https://doi.org/10.1088/2041-8205/709/2/L172)
- Saccardi, A., Kann, D. A., Palmerio, J., et al. 2023, *GRB Coordinates Network*, 33281, 1
- Sánchez-Ramírez, R., Lang, R. G., Pozanenko, A., et al. 2024, *A&A*, 692, A3, doi: [10.1051/0004-6361/202449783](https://doi.org/10.1051/0004-6361/202449783)
- Santana, R., Barniol Duran, R., & Kumar, P. 2014, *ApJ*, 785, 29, doi: [10.1088/0004-637X/785/1/29](https://doi.org/10.1088/0004-637X/785/1/29)
- Sari, R., & Piran, T. 1999, 520, 641, doi: [10.1086/307508](https://doi.org/10.1086/307508)
- Sari, R., Piran, T., & Narayan, R. 1998, *ApJL*, 497, L17, doi: [10.1086/311269](https://doi.org/10.1086/311269)
- Sarin, N., Hübner, M., Omand, C. M. B., et al. 2024, *MNRAS*, 531, 1203, doi: [10.1093/mnras/stae1238](https://doi.org/10.1093/mnras/stae1238)
- Sault, R. J., Teuben, P. J., & Wright, M. C. H. 1995, in *Astronomical Society of the Pacific Conference Series*, Vol. 77, *Astronomical Data Analysis Software and Systems IV*, ed. R. A. Shaw, H. E. Payne, & J. J. E. Hayes, 433. <https://arxiv.org/abs/astro-ph/0612759>
- Serino, M., Iwakiri, W., Negoro, H., et al. 2023, *GRB Coordinates Network*, 33265, 1
- Sharma, V., Iyyani, S., Bhattacharya, D., et al. 2020, *MNRAS*, 493, 5218, doi: [10.1093/mnras/staa570](https://doi.org/10.1093/mnras/staa570)
- Smartt, S. J., Smith, K. W., Srivastav, S., et al. 2023, *GRB Coordinates Network*, 33278, 1
- Spada, M., Panaitescu, A., & Mészáros, P. 2000, *ApJ*, 537, 824, doi: [10.1086/309048](https://doi.org/10.1086/309048)
- Starling, R. L. C., van der Horst, A. J., Rol, E., et al. 2008, *ApJ*, 672, 433, doi: [10.1086/521975](https://doi.org/10.1086/521975)
- Stetson, P. B. 1987, *PASP*, 99, 191, doi: [10.1086/131977](https://doi.org/10.1086/131977)
- Sugita, S., Kawai, N., Nakahira, S., et al. 2018, *PASJ*, 70, 81, doi: [10.1093/pasj/psy076](https://doi.org/10.1093/pasj/psy076)
- Sugizaki, M., Mihara, T., Serino, M., et al. 2011, *PASJ*, 63, 635. <https://arxiv.org/abs/1102.0891>
- Swain, V., Kumar, H., Waratkar, G., et al. 2023, *GRB Coordinates Network*, 33269, 1
- Tody, D. 1986, in *Society of Photo-Optical Instrumentation Engineers (SPIE) Conference Series*, Vol. 627, *Instrumentation in astronomy VI*, ed. D. L. Crawford, 733, doi: [10.1117/12.968154](https://doi.org/10.1117/12.968154)
- Tody, D. 1993, in *Astronomical Society of the Pacific Conference Series*, Vol. 52, *Astronomical Data Analysis Software and Systems II*, ed. R. J. Hanisch, R. J. V. Brissenden, & J. Barnes, 173
- Tohuvavohu, A., Kennea, J. A., DeLaunay, J., et al. 2020, *ApJ*, 900, 35, doi: [10.3847/1538-4357/aba94f](https://doi.org/10.3847/1538-4357/aba94f)
- Troja, E., Lipunov, V. M., Mundell, C. G., et al. 2017, *Nature*, 547, 425, doi: [10.1038/nature23289](https://doi.org/10.1038/nature23289)
- van Eerten, H., & MacFadyen, A. 2013, *ApJ*, 767, 141, doi: [10.1088/0004-637X/767/2/141](https://doi.org/10.1088/0004-637X/767/2/141)
- van Paradijs, J., Groot, P. J., Galama, T., et al. 1997, *Nature*, 386, 686, doi: [10.1038/386686a0](https://doi.org/10.1038/386686a0)
- Vianello, G., Lauer, R. J., Younk, P., et al. 2015, *arXiv e-prints*, arXiv:1507.08343. <https://arxiv.org/abs/1507.08343>
- Vurm, I., Beloborodov, A. M., & Poutanen, J. 2011, *ApJ*, 738, 77, doi: [10.1088/0004-637X/738/1/77](https://doi.org/10.1088/0004-637X/738/1/77)
- Wang, X.-G., Zhang, B., Liang, E.-W., et al. 2015, *ApJS*, 219, 9, doi: [10.1088/0067-0049/219/1/9](https://doi.org/10.1088/0067-0049/219/1/9)
- Wang, X.-G., Zhou, J.-W., Zhou, Z.-M., et al. 2024, *ApJ*, 969, 146, doi: [10.3847/1538-4357/ad463f](https://doi.org/10.3847/1538-4357/ad463f)
- Waratkar, G., Navaneeth, P. K., Shetty, P., et al. 2023, *GRB Coordinates Network*, 33268, 1
- Yonetoku, D., Murakami, T., Nakamura, T., et al. 2004, *ApJ*, 609, 935, doi: [10.1086/421285](https://doi.org/10.1086/421285)
- Zhang, B., & Kobayashi, S. 2005, *ApJ*, 628, 315, doi: [10.1086/429787](https://doi.org/10.1086/429787)
- Zhang, B., & Mészáros, P. 2001, *ApJL*, 552, L35, doi: [10.1086/320255](https://doi.org/10.1086/320255)
- Zhang, B., & Pe'er, A. 2009, *ApJL*, 700, L65, doi: [10.1088/0004-637X/700/2/L65](https://doi.org/10.1088/0004-637X/700/2/L65)
- Zhang, B., & Yan, H. 2011, *ApJ*, 726, 90, doi: [10.1088/0004-637X/726/2/90](https://doi.org/10.1088/0004-637X/726/2/90)